Acta Pharmaceutica Sinica B 2022;12(1):406–423

Chinese Pharmaceutical Association
Institute of Materia Medica, Chinese Academy of Medical Sciences

Acta Pharmaceutica Sinica B

www.elsevier.com/locate/apsb
www.sciencedirect.com

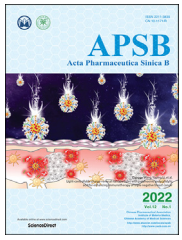

ORIGINAL ARTICLE

Multi-responsive nanotheranostics with enhanced tumor penetration and oxygen self-producing capacities for multimodal synergistic cancer therapy

Shuangquan Gou[a,b,c,†], Nanxi Chen[b,†], Xiaoai Wu[d,†], Menghang Zu[b,c], Shixiong Yi[b], Binwu Ying[e,*], Fangyin Dai[b], Bowen Ke[a,*], Bo Xiao[b,c,*]

[a]*Laboratory of Anesthesiology & Critical Care Medicine, Department of Anesthesiology, West China Hospital, Sichuan University, Chengdu 610041, China*
[b]*State Key Laboratory of Silkworm Genome Biology, College of Sericulture, Textile and Biomass Sciences, Southwest University, Chongqing 400715, China*
[c]*Chongqing Key Laboratory of Soft-Matter Material Chemistry and Function Manufacturing, School of Materials and Energy, Southwest University, Chongqing 400715, China*
[d]*Department of Nuclear Medicine, West China Hospital, Sichuan University, Chengdu 610041, China*
[e]*Department of Laboratory Medicine, West China Hospital, Sichuan University, Chengdu 610041, China*

Received 5 March 2021; received in revised form 5 May 2021; accepted 26 May 2021

KEY WORDS

Quadruple responsibility;
Silk fiborin;
Nanotheranostic;
Oxygen self-generation;
Mitochondrial targeting;
Phototherapy;
Chemotherapy;
Cancer

Abstract Incorporation of multiple functions into one nanoplatform can improve cancer diagnostic efficacy and enhance anti-cancer outcomes. Here, we constructed doxorubicin (DOX)-loaded silk fibroin-based nanoparticles (NPs) with surface functionalization by photosensitizer (N770). The obtained nanotheranostics (N770-DOX@NPs) had desirable particle size (157 nm) and negative surface charge (−25 mV). These NPs presented excellent oxygen-generating capacity and responded to a quadruple of stimuli (acidic solution, reactive oxygen species, glutathione, and hyperthermia). Surface functionalization of DOX@NPs with N770 could endow them with active internalization by cancerous cell lines, but not by normal cells. Furthermore, the intracellular NPs were found to be preferentially retained in mitochondria, which were also efficient for near-infrared (NIR) fluorescence imaging, photothermal imaging, and photoacoustic imaging. Meanwhile, DOX could spontaneously accumulate in the nucleus. Importantly, a mouse test group treated with N770-DOX@NPs plus NIR irradiation achieved the best tumor

*Corresponding authors.
E-mail addresses: yingbinwu@scu.edu.cn (Binwu Ying), bowenke@scu.edu.cn (Bowen Ke), bxiao@swu.edu.cn (Bo Xiao).
[†]These authors made equal contributions to this work.
Peer review under responsibility of Chinese Pharmaceutical Association and Institute of Materia Medica, Chinese Academy of Medical Sciences.

https://doi.org/10.1016/j.apsb.2021.07.001
2211-3835 © 2022 Chinese Pharmaceutical Association and Institute of Materia Medica, Chinese Academy of Medical Sciences. Production and hosting by Elsevier B.V. This is an open access article under the CC BY-NC-ND license (http://creativecommons.org/licenses/by-nc-nd/4.0/).

retardation effect among all treatment groups based on tumor-bearing mouse models and a patient-derived xenograft model, demonstrating the unprecedented therapeutic effects of trimodal imaging-guided mitochondrial phototherapy (photothermal therapy and photodynamic therapy) and chemotherapy. Therefore, the present study brings new insight into the exploitation of an easy-to-use, versatile, and robust nanoplatform for programmable targeting, imaging, and applying synergistic therapy to tumors.

© 2022 Chinese Pharmaceutical Association and Institute of Materia Medica, Chinese Academy of Medical Sciences. Production and hosting by Elsevier B.V. This is an open access article under the CC BY-NC-ND license (http://creativecommons.org/licenses/by-nc-nd/4.0/).

1. Introduction

Stimuli-responsive nanoscale drug delivery systems (NDDSs), which possess the capacity to yield triggered responses upon stimulation with specific physiological or external factors [*e.g.*, pH, reactive oxygen species (ROS), enzymes, and hyperthermia], have been developed for spatial and temporal on-demand drug release[1,2]. Since various environmental factors in tumor often change simultaneously, single stimulus-responsive NDDSs are inefficient in controlled drug release[3,4]. Accumulating evidence confirms that NDDSs responding to multiple stimuli display superior tumor-specific drug release performance compared with the single-stimulus-responsive ones, resulting in improved chemotherapeutic efficacies and reduced side effects[5]. The conventional approaches to attain multi-responsive NDDSs are to bring numerous responsive chemical groups together by complicated chemical reactions[6]. However, these chemical processes often involve heavy-metal catalysts, organic solvents, and relatively extreme reaction conditions, leading to high cost, potential toxicity, and environmental pollution[7,8].

Regenerated silk fibroin (RSF) is a biocompatible and biodegradable macromolecule, which can easily be processed into nanoparticles (NPs) in a mild environment (*e.g.*, room temperature, regular organic solvents, and regular saline solution)[9]. Recently, Kaplan's group[10] was the first to report that the drug release profiles of RSF-based NDDSs were pH-dependent. They found that the amount of drugs accumulatively released from NDDSs was remarkably higher in acidic buffer (pH 4.5) than in neutral buffer (pH 7.4). Very recently, Gou et al.[11,12] not only verified the pH-responsive property of these RSF-based NDDSs, but also found that they had obvious hydrogen peroxide (H_2O_2)/glutathione (GSH) responses. Furthermore, they discovered the potential mechanism responsible for their reactivity to pH/ROS/GSH. The hydrogen ions and H_2O_2 molecules were found to break the hydrogen bonds and van der Waals force in the hydrophobic β-sheet structures, and GSH could reduce the intermolecular and intramolecular disulfide bonds into sulfhydryl groups. Therefore, treatment with hydrogen ions, H_2O_2, and GSH loosens the compact structure of RSF-based NDDSs, resulting in the acceleration of drug release from these NDDSs to diseased sites.

Considering that tumors have multi-level variabilities and complexities, the combination of chemotherapy and other therapeutic modalities has attracted huge research interest for cancer treatment[13,14]. Phototherapy, including photothermal therapy (PTT) and photodynamic therapy (PDT), has emerged as one of the most promising therapeutic modalities due to its advantageous features such as noninvasiveness, spatiotemporal control, high therapeutic efficacy, and negligible drug resistance, as well as low side effects[15,16]. The combined application of chemotherapy and phototherapy in cancer treatment could augment the tumoricidal efficacy of chemotherapeutic drugs with the synergistic effects of phototherapy[17,18]. Generally, drugs exert their therapeutic roles within or surrounding certain organelles[19]. Mitochondria are critical organelles in eukaryotic cells, which are closely associated with various cellular processes, including energy supply, calcium homeostasis, and cell apoptosis[20]. Thus, mitochondrial dysfunction has been an effective approach to induce cell death[21]. The hyperthermia is produced by PTT dispersed in the cytoplasm, and the generated singlet oxygen ($^1O_2$) has a short lifespan (~40 ns) and restricted diffusion radius (<30 nm), so the damages caused by phototherapy-induced hyperthermia and $^1O_2$ are spatially and temporally restricted[22,23]. Therefore, new investigations are required for the development of photosensitizers (PSs) targeting mitochondria of tumor cells[24]. Although mitochondria-targeted delivery of PS molecules can be actualized by the surface modification of several moieties (*e.g.*, protein transduction domains, triarylphosphonium cations, and lipophilic cations), these PS derivatives still lack tumor cell-targeted properties[25,26]. Wang et al.[27] screened a multifunctional heptamethine cyanine-based PS (N770), which could be specifically accumulated in tumor cells by organic anion-transporting polypeptide (OATP)-mediated active transport and preferentially aggregated in mitochondria *via* a "structure-inherent targeting strategy". Moreover, this tumor cell mitochondria-targeting N770 also integrated the functions of PDT, PTT, near-infrared (NIR) fluorescence imaging (FLI), photothermal imaging (PTI), and photoacoustic imaging (PAI). However, to the best of our knowledge, no attempt has been conducted to take advantage of the overall functions of N770 in nanotheranostics so far.

In this study, we aimed to develop an easily fabricated NDDS with numerous features of quadruple responsiveness, dual level-targeted drug delivery, multimodal imaging, self-production of oxygen (O_2), tumor cell mitochondrial phototherapy, and chemotherapy. Firstly, we loaded the antitumor drug doxorubicin (DOX) in RSF-based NPs, and further functionalized their surface with N770. Thereafter, the multiple responsiveness of the obtained N770-DOX@NPs to treatment with acidic solution, ROS, GSH, and hyperthermia was investigated. Their tumor cell mitochondria-targeting capacity was confirmed in different kinds of tumor cell lines. To guide the phototherapy, multimodal imaging was carried out to visually locate the tumor sites. Finally, the *in vitro* and *in vivo* synergies of combined treatment with mitochondrial phototherapy and chemotherapy were verified.

2. Materials and methods

2.1. Fabrication of N770-DOX@NPs

RSF was extracted and purified according to previous reports[11,28]. The obtained RSF was dissolved in water (1.5%, *w/v*), and DOX

(0.5 mg/mL) was dissolved in RSF solution. The RSF/DOX solution was dropped into acetone with gentle stirring, and the mixture became an emulsion immediately. The emulsion was vortexed for 30 s, placed in an ice bath, and sonicated for 1 min at amplitude of 30%. After stirring in ventilated facility for 2 h, the obtained DOX-NPs were collected by centrifugation at 13,000×*g* for 20 min using a Beckman Coulter Avanti J-26S XPI Centrifuge (Beckman Coulter, Brea, CA, USA), washed 3 times with water, lyophilized, and stored at −20 °C.

Conjugation of *N*-hydroxysuccinimide-N770 (NHS-N770) molecules to the surface of DOX-NPs was carried out by the chemical reaction between carboxyl groups of NHS-N770 and amino groups of RSF. Briefly, NHS-N770 solution (1 mg/mL) was prepared, and mixed with the obtained DOX-NP suspension in a sodium acetate/acetic acid buffer (pH 6.0). Subsequently, the chemical reaction was carried out at room temperature. After reaction for 4 h, N770-functionalized NPs were collected by centrifugation at 13,000×*g* for 20 min using a Beckman Coulter Avanti J-26S XPI Centrifuge, washed 3 times with water to remove unreacted NHS-N770, lyophilized, and stored at −20 °C.

2.2. *In vitro cellular uptake profiles of N770-DOX@NPs*

Cells were seeded in 8-well plates (BD Falcon, Bedford, MA, USA) at a cell density of 1×10^5 cells per well, and cultured overnight at 37 °C. After that, the complete media were replaced with basic media containing various samples with the equal N770 concentration (50 μg/mL). After co-incubation for predetermined time intervals (1, 2 and 4 h), cells were thoroughly rinsed with cold PBS to eliminate the residual NPs, and fixed in formalin solution for 30 min. Alexa Fluor 633-labeled phalloidin was applied to stain cytoskeleton for 1 h, followed by staining nuclei with 4′,6-diamidino-2-phenylindole (DAPI). Cells were imaged using a confocal laser scanning microscope (CLSM, Zeiss-800, Jena, Germany).

Cells were grown in 12-well plates at a cell density of 3×10^5 cells per well and cultured overnight at 37 °C. After that, the complete media were replaced with basic media containing various samples with the equal N770 concentration (50 μg/mL). After co-incubation for predetermined time intervals (1, 2, and 4 h), cells were thoroughly rinsed with cold PBS to eliminate the residual NPs, which were not internalized. Subsequently, cells were harvested using a cell scraper, transferred to polystyrene test tubes, and suspended in flow cytometry (FCM) buffer. The quantification of the cellular uptake efficiencies of various samples were performed on a FCM (Biosciences, ACEA NovoCyte™, San Diego, USA) using a FITC channel.

2.3. *Targeting mechanism of N770-DOX@NPs*

A549 cells were seeded in 6-well plates at a cell density of 2×10^5 cells per well and incubated overnight. Thereafter, cells were subjected to different treatments before the incubation of various NPs as follow: cells were incubated at ice bath for 30 min to disturb the production of ATP; cells were incubated with chlorpromazine (10 μg/mL) or methyl-β-cyclodexrin (MβCD, 7.5×10^{-6} mol/L) for 1 h to hinder the endocytic pathway; cells were incubated with sulfobromophthalein (BSP, 250×10^{-6} mol/L) for 5 min to evaluate the effect of OATP transporters. After different treatments, cells were then incubated with N770-DOX@NPs for 4 h. Finally, the fluorescent images were analyzed by a CLSM (Zeiss).

2.4. *In vitro phototherapy*

A549 cells were seeded in 96-well plates at a cell density of 3.0×10^4 cells per well and cultured overnight at 37 °C. In the context of the NIR irradiation groups, cells were treated with various samples for 4 h. After that, these cells were exposed to NIR laser (808 nm, 1.5 W/cm^2) for 5 min and further incubated for 24 or 48 h, respectively. Cells without treatment were treated as a negative control, whereas Triton X-100 (0.5%, *w*/*v*)-treated cells were used a positive control. Cell viability was determined using 3-(4,5-dimethylthiazol-2-yl)-2,5-diphenyl tetrazolium bromide (MTT) assay.

Single effect of PDT or PTT alone was investigated according to the protocol as reported before[29]. Ice bath and pretreatment with *N*-acetyl-L-cysteine (NAC) were used to offset hyperthermia and elimination of ROS, respectively, during laser irradiation. Briefly, A549 cells were seeded in 6-well plates at a cell density of 1×10^6 cells per well and cultured overnight at 37 °C. After that, cells were treated with N770-DOX@NPs (N770, 10 μg/mL) for 4 h. The PTT alone group, PDT alone group, and synergistic PTT/PDT group were irradiated by NIR laser (808 nm, 1.5 W/cm^2) for 5 min. After incubation for 4 h, cells were stained with calcein-(acetoxymethyl) AM and propidium iodide (PI) for visualization of live and dead/late apoptosis cells, respectively. The fluorescent images of cells were acquired using a biological inverted microscope (Olympus IX71, Tokyo, Japan).

2.5. *Tumor model*

Athymic nude mice were used in the animal experiments. All mice were purchased from Chongqing Tengxin Biotechnologies Company (Chongqing, China). All the animal care and experiment protocols were in accordance with the Southwest University Institutional Care and Use Committee. Mice were housed in standard mouse cages with libitum access to water and food, and they were acclimatized for at least a week before further experiments. Athymic nude mice bearing subcutaneous tumor models were established by subcutaneous injection of A549 cells or 4T1 cells onto the dorsa of mice (6—7 weeks old). Briefly, 1×10^7 cells suspended in PBS (100 μL) were injected into the dorsa of mice. After that, mice were housed in standard cages, and tumor volumes were recorded every day. Tumor volumes were calculated by the following Eq. (1)

$$\text{Volume} = \frac{\text{Length} \times \text{Width}^2}{2} \quad (1)$$

2.6. *In vivo evaluation of anti-cancer outcomes*

A549 lung tumor xenograft mouse model and 4T1 breast tumor xenongraft mouse model were established by subcutaneous injection of A549 cells or 4T1 cells onto the dorsa of mice. In terms of patient-derived xenograft (PDX) studies, mice were implanted with tumor tissues from patients with lung cancers. Mice in various drug-treated groups were intravenously injected with PBS (200 μL), free DOX solution (3 mg/kg, 200 μL), free N770 solution (2.13 mg/kg, 200 μL) or NPs (equivalent N770 = 2.13 mg/kg or DOX concentration = 3 mg/kg, 200 μL) every 2 days for a total of 2 doses. Twenty-four hours after injection, tumors in the irradiation mouse groups were exposed to an 808 nm laser at a power density of 0.8 W/cm^2 for 5 min. Body weights and tumor volumes

were recorded during the whole experiments. The relative tumor volumes were calculated as V/V_0 (V_0 represent the volume at the beginning of the treatment; V represent the real-time volume post irradiation during the treatment). After three cycle irradiation, tumors were collected, fixed in 10% formaldehyde, and embedded in paraffin. The tissue sections (5 μm) were stained with Hematoxylin & Eosin (H&E), Ki67, and terminal deoxynucleotidyl transferase-mediated nick end labeling (TUNEL) kits, respectively. The survival rates of tumor-bearing mice in each treatment groups were monitored during the whole experiment.

2.7. *Evaluation of systemic safety of NPs in mice*

In vivo hemocompatibility of NPs was assessed using a hematology analyzer (Mindray BC-2600; Mindray Biomedical Electronics Co., Ltd., Shenzhen, Guangdong, China). BALB/c mice (10-week old) were intravenously injected with NPs (the concentration of N770 = 10 mg/kg). Body weight was recorded every two days over 20 days of experiment. At the desired time point (1, 5, 10, and 20 days), mice blood was harvested and analyzed using a hematology analyzer. Meanwhile, the quantification of biochemical markers related to liver/kidney functions was determined in plasma by the relevant assay kits. At the end of time point, mice were euthanized. Major organs (heart, liver, spleen, lung, and kidney) were isolated and weighed, and the organ index was calculated. As to histological examination, major organs were fixed in buffered formalin, embedded in paraffin, cut at a thickness of 5 μm, and further stained with H&E kit.

3. Results and discussion

3.1. *Synthesis and physicochemical characterization*

The cyanine dye with the lyophilic cationic moiety as its core structure was chemically produced by conjugating the *N*-alkyl side to the heptamethine structure, and further conjugated with NHS. The obtained compound was named NHS-N770 (Supporting Information Scheme S1), and its structure was confirmed by ^{1}H NMR. RSF was extracted, purified, and used for the fabrication of RSF-based NPs. As reported, sericin alone or silk fibroin-linked sericin showed significant immunogenicity and opsonization[30,31]. Thus, the degree of degumming is a key parameter for the quality control of RSF. Here, a direct visual method was used to evaluate the result of the degumming. It was found that partially degummed silk fibroin fiber exhibited a rough surface (Supporting Information Fig. S1A), whereas completely degummed fiber had a smooth surface and clear lineament (Fig. S1B). Moreover, sodium dodecyl sulfate-polyacrylamide gel electrophoresis (SDS-PAGE) was carried out to verify the homogeneity of RSF, as shown in Fig. S1C.

Next, RSF-based NPs (blank NPs and DOX@NPs) were fabricated using an optimized desolvation method, and their surface was further functionalized by NHS-N770 through the chemical reaction between the amino groups of RSF molecules and the NHS groups of NHS-N770. A schematic illustration of N770-DOX@NPs is presented in Fig. 1A. The scanning electron microscope (SEM) image revealed that N770-DOX@NPs had a spherical morphology with a rough surface (Fig. 1B), and their average particle size was approximately 100.2 nm, which was smaller than the hydrodynamic particle size value (157.4 nm) determined by dynamic light scatting (DLS). Due to the shrinkage of N770-DOX@NPs in the air-drying process, their average particle size determined by SEM observation was much smaller than that measured by DLS. Besides, we found that these NPs showed a narrow size distribution with a polydispersity index (PDI) value less than 0.101 (Supporting Information Fig. S2A). As summarized in Supporting Information Table S1, zeta potentials of the blank NPs and DOX@NPs were negative (around −13.0 mV). However, after adding N770 to the surface of DOX@NPs, the obtained N770-DOX@NPs showed a zeta potential of −25.7 mV, suggesting the successful conjugation of N770 to the NP surface. It was found that the DOX loading amounts and the encapsulation efficiencies of both DOX@NPs and N770-DOX@NPs were 3.1 and 74%, respectively. The amount of N770 grafted to the surface of N770-DOX@NPs was 27.6 μg/mg, and its grafting efficiency was as high as 87.3%.

To examine the aqueous stability of N770-DOX@NPs, we studied the changes in their hydrodynamic particle sizes (Fig. 1C) and zeta potentials (Fig. 1D) in various simulated biological fluids [phosphate-buffered saline (PBS), Dulbecco's modified Eagle's medium (DMEM), and 10% serum]. The hydrodynamic particle sizes of N770-DOX@NPs slightly increased after 7 days of incubation in different biological environments. Their surface charges remained stable in PBS and DMEM, and showed little increase when incubated in serum, revealing that these NPs could maintain their stability in extracellular environments. In addition, it was found that N770-DOX@NPs were suspended in aqueous solution (Fig. S2B). As observed in Supporting Information Fig. S3, the characteristic peaks in the UV−Vis−NIR spectrum of N770-DOX@NPs are broadened compared with those of free DOX and free N770 at the same DOX/N770 concentrations. In addition, their intensities were markedly weaker than those of free DOX and free N770. These findings can be ascribed to the aggregation of DOX and N770 in N770-DOX@NPs. Furthermore, N770-DOX@NPs exhibited an obvious optical absorption ranging from 700 to 900 nm.

RSF can easily be switched from the dissolved state to the solid state by regulation of the conformational change. During the fabrication process of N770-DOX@NPs, the desolvation procedure destroys the hydration layer of RSF, which induces the aggregation of RSF molecules and the formation of NPs at the proper RSF concentrations. To determine the conformational transition of RSF molecules, various measurement techniques were applied. As can be seen in Supporting Information Fig. S4, several sharp absorption peaks, registered at 1650 (amide I), 1534 (amide II), and 1250 cm^{-1} (amide III), were detected in the Fourier transform infrared (FTIR) spectrum of RSF. These data clearly indicate that RSF molecules have random coils and amorphous structures. Moreover, when compared with the FTIR spectrum of RSF, N770 and N770-DOX@NPs showed sharp peaks at 1149 and 1070 cm^{-1}, which were ascribed to the C−O absorption peak of furanose rings and the variable vibration absorption peak of aldehyde hydroxyl. These findings confirm the successful conjugation of N770 molecules to the surface of DOX@NPs. Furthermore, clear absorption peaks of amide bonds were observed in the FTIR spectra of both blank NPs and N770-DOX@NPs, demonstrating the conformation transition in the process of forming NPs.

RSF shows a negative peak at 207 nm in its circular dichroism (CD) spectrum (Fig. 1E). However, this peak was replaced by a negative peak at 222 nm and a positive peak located at 195 nm, suggesting that the conformation of RSF molecules transited from random coils to β-structures. The corresponding quantitative results in Fig. 1F showed that the amount of β-structures in N770-DOX@NPs was approximately

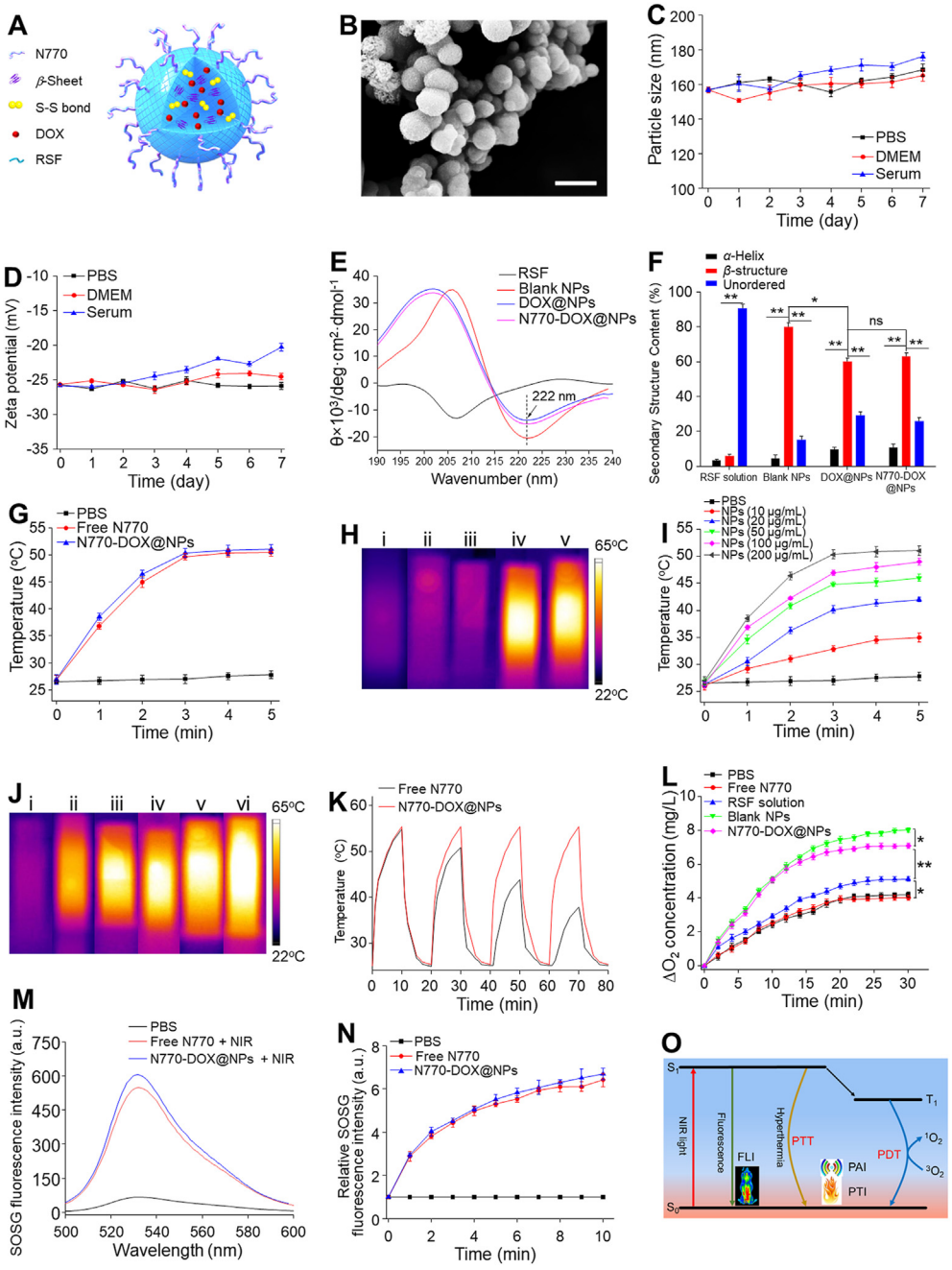

Figure 1 Physicochemical properties of various NPs. (A) Schematic illustration and (B) SEM image of N770-DOX@NPs. Scale bar is 200 μm. Changes of (C) particle sizes and (D) zeta potentials of N770-DOX@NPs during incubation in various buffers for 7 days. (E) CD spectra and (F) the corresponding contents of secondary structures N770 in various samples. (G) Temperature rise behaviors of PBS, free N770 solution and N770-DOX@NP suspension. (H) Thermographic images of cuvettes containing (i) PBS, (ii) free DOX solution, (iii) DOX@NP suspension, (iv) free N770 solution, and (v) N770-DOX@NP suspension at an equal N770 concentration of 200 μg/mL under NIR laser irradiation (1.5 W/cm^2, 5 min). (I) Temperature rise profiles and (J) the corresponding thermographic images of N770-DOX@NP suspensions with different N770 concentrations under NIR laser irradiation (1.5 W/cm^2, 5 min). (K) Temperature variations of free N770 solution and N770-DOX@NP suspension exposed to NIR laser irradiation (1.5 W/cm^2). (L) O_2 generation profiles of H_2O_2 solutions treated with various samples. (M) Singlet oxygen generation profiles of free N770 solution and N770-DOX@NP suspension determined by SOSG fluorescence intensities under NIR irradiation. (N) Variations of SOSG fluorescence intensities of free N770 solution and N770-DOX@NP suspension within 10 min upon NIR irradiation. (O) Illustration of photophysical processes of N770-DOX@NPs. Data are expressed as mean ± SEM ($n = 3$; $^*P < 0.05$; $^{**}P < 0.01$; and ns = not significant).

9.7-fold higher than that of RSF molecules. In addition, the percentage of β-structures in N770-DOX@NPs was remarkably lower than that in blank NPs, revealing that the loading of DOX into NPs would influence the conformational transition of RSF molecules during the formation of NPs. These results collectively imply that the transformation from random coils to β-structures occurs during the desolvation procedure, and that N770-DOX@NPs with compact Silk II structures are successfully obtained.

3.2. *Photo-induced properties*

Next, the photothermal conversion efficiency and photodynamic properties of N770-DOX@NPs were studied. Fig. 1G and H shows that the temperature of free N770 solution was swiftly boosted to 51.4 °C after NIR laser irradiation for 5 min. Interestingly, a N770-DOX@NP suspension showed an increase in temperature comparable to that of free N770 solution under the same irradiation conditions, implying the efficient photothermal conversion property of N770-DOX@NPs. Besides, we found that the NIR-induced rises in temperature depended on the concentration of N770-DOX@NPs (Fig. 1I and J). Furthermore, the photothermal stability of N770 in N770-DOX@NPs after repeated NIR irradiation was assessed. It was obvious from Fig. 1K that after repeating the irradiation four times, free N770 solution underwent clear decreases in the maximum temperature attained, whereas the maximum elevated temperature of the N770-DOX@NP suspension showed negligible changes, which showed that the conjugation of N770 to the surface of NPs could greatly enhance its photothermal stability.

A sufficient O_2 supply is required for effective PDT[32]. To evaluate the O_2 generation potential of N770-DOX@NPs in the tumor microenvironment (TME), the O_2 content in various sample-treated H_2O_2 solutions was compared. As shown in Fig. 1L, the O_2 content in the RSF-treated group was much higher than that of the PBS control group and the group treated with free N770, indicating that RSF molecule intrinsically catalyzes H_2O_2. Moreover, it was found that blank RSF-based NPs had the strongest O_2-generating capacity among all the treatment groups. These findings reveal that the processing of RSF molecules into RSF-based NPs could enhance their H_2O_2 catalytic properties. We also found that the N770-DOX@NP-treated group showed a slightly lower O_2 content compared to the blank RSF-based NP-treated group, demonstrating the effective and intrinsic O_2 generation property of N770-DOX@NPs.

N770 is an effective PS, and it can produce a large amount of $^1O_2$, which can destroy tumor cells upon NIR irradiation. Herein, the photodynamic properties of N770 and N770-DOX@NPs were comparatively investigated by determining the generated amounts of $^1O_2$. After 10 min of irradiation, the fluorescence intensity of singlet oxygen sensor green (SOSG) fluorescent probe in N770-DOX@NPs was identical to that of free N770 solution (Fig. 1M). We also found that the generated amounts of ROS increased with the prolongation of NIR irradiation time (Fig. 1N), demonstrating that chemically conjugating N770 to the NP surface could maintain its photodynamic property. The overall photophysical processes of N770-DOX@NPs are illustrated in Fig. 1O.

3.3. *Quadruple responsive drug release*

The drug release behaviors of N770-DOX@NPs were determined by a traditional dialysis method. Since DOX could maintain stable in various environments (Supporting Information Fig. S5), it was utilized as a model drug in the present study. As drugs had to go through various biological environments with different pH values, the release profiles of DOX from N770-DOX@NPs were investigated in buffers with different pH values. We prepared buffers with pH values of 7.4, 6.8, 6.0, and 4.5, which corresponded to the pH values in blood (pH 7.4), early endosomes (pH 6.0−6.8), and late lysosomes (pH 4.5), respectively. Fig. 2A reveals that the DOX release rate from N770-DOX@NPs clearly increased with the decreases in the pH values of the buffers. In particular, around 41.4% of DOX was accumulatively released from N770-DOX@NPs after 6-day incubation in the buffer with a pH value of 7.4, while the percentage of DOX released from NPs in the presence of buffer with a pH value of 4.5 reached 76.7% after incubation for the same duration.

It is known that tumor tissues tend to produce large amounts of ROS due to the Warburg effect[33], and thus, we evaluated the ROS-responsive properties of N770-DOX@NPs. As seen in Fig. 2B, the DOX release rate from N770-DOX@NPs in the buffers (pH 7.4) increased with the addition of H_2O_2 when compared with that in the buffer (pH 7.4) without H_2O_2. We also found that the release rates of DOX from NPs clearly increased with increasing H_2O_2 concentrations. Particularly, after incubation of N770-DOX@NPs in buffer (pH 7.4; 1 mmol/L H_2O_2) for 6 days, the cumulative DOX release percentage reached as high as 90.4%, suggesting the obvious H_2O_2-responsive property of N770-DOX@NPs.

Many disulfide linkages exist in RSF-based NPs[6], and they are therefore expected to show a GSH-responsive drug release profile. Fig. 2C shows that the DOX release rates from NPs were GSH concentration-dependent, increasing remarkably with an increase of the GSH concentration. The cumulative DOX release percentage in buffer (pH 7.4; GSH, 10 mmol/L) was remarkably higher (72.4%) than that observed in GSH-free buffer (pH 7.4), which could be ascribed to the cleavage of disulfide bonds in N770-DOX@NPs, leading to the disintegration of the internal structures of NPs.

As hyperthermia was generated upon the irradiation of PSs[34], the impact of hyperthermia on the release rates of DOX from N770-DOX@NPs was evaluated. After incubation in buffer (pH 7.4) for 6 days, the cumulative release percentage of DOX from N770-DOX@NPs reached 60.5% at 50 °C, which was remarkably higher than that at 37 °C (Fig. 2D). It can easily be found that the DOX release rates of N770-DOX@NPs increased upon increasing the environmental temperature.

Since multiple stimulating factors co-exist in TME[35], the synergistic effects of these factors on drug release profiles were evaluated. As shown in Fig. 2E, when the H_2O_2 concentration of the buffer with a pH value of 6.0 was set at 1 mmol/L, the DOX release rate from N770-DOX@NPs was significantly higher than that in the pH 7.4 buffer (H_2O_2, 1 mmol/L), indicating the obvious synergistic effects of pH and ROS on the release rate of DOX from N770-DOX@NPs. Also, the combination of acidic pH with GSH (Fig. 2F) or hyperthermia (Fig. 2G) greatly augmented the DOX release rates from N770-DOX@NPs, in comparison with the individual stimuli. Importantly, a cascade stimulation process of various stimuli was constructed to estimate the multi-responsive drug release. As displayed in Fig. 2H, the release rate of DOX from N770-DOX@NPs was remarkably increased in buffers with multiple stimulating factors when compared with that in the control buffer with a pH value of 7.4. It is worth noting that the enhanced drug release property of NIR irradiation could be ascribed to the ROS and hyperthermia produced by N770-

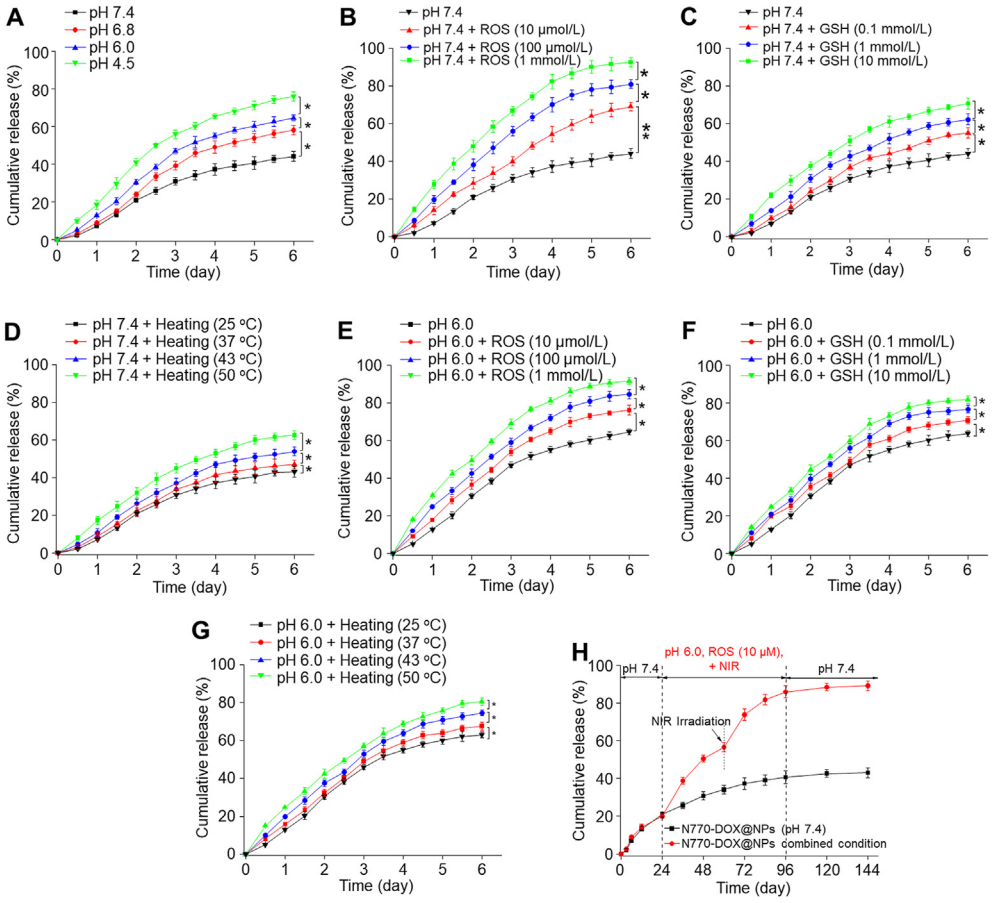

Figure 2 *In vitro* multi-responsive release profiles of DOX from N770-DOX@NPs. Cumulative release profiles of DOX from N770-DOX@NPs in various releasing buffers with (A) different pH values (7.4, 6.8, 6.0, and 4.5). Cumulative release profiles of DOX from N770-DOX@NPs in releasing buffers (pH 7.4) with (B) different ROS concentrations (10 μmol/L, 100 μmol/L, and 1 mmol/L), (C) different GSH concentrations (0.1, 1, and 10 mmol/L), and (D) different temperatures (25, 37, 43, and 50 °C). Cumulative release profiles of DOX from N770-DOX@NPs in releasing buffer (pH 6.0) with (E) different ROS concentrations (10 μmol/L, 100 μmol/L, and 1 mmol/L), (F) different GSH concentrations (0.1, 1, and 10 mmol/L), and (G) different temperatures (25, 37, 43, and 50 °C). (H) Cumulative release profiles of DOX from N770-DOX@NPs in the releasing buffers with gradual changes of the releasing environments. Data are expressed as mean ± SEM ($n = 3$; $^*P < 0.05$; $^{**}P < 0.01$; and ns = not significant).

DOX@NPs upon NIR irradiation. Overall, these results indicate that the RSF-based NPs can respond to specific environmental factors and clearly exhibit multi-responsiveness.

Disrupting the structure has an impact on the drug release profiles of NDDSs. In the context of RSF-based NPs, the β-sheet regions and disulfide bonds dominated their main physicochemical properties. Recent studies demonstrated that factors destroying the hydrogen bonds (*e.g.*, hydrogen ions, H_2O_2 molecules, and hyperthermia) and disulfide bonds (GSH) could loosen the compact structure of RSF-based drug carriers, resulting in acceleration of the release rates of drugs from these carriers. Together, RSF-based NPs possess multi-responsive drug release behaviors, and have the capacity to achieve desired release kinetics in the TME and/or under external NIR treatment.

3.4. *In vitro evaluation of programmed drug delivery*

The purpose of drug delivery is to transport bio-active drugs to targeted cell organelles with a controlled release style and in a reasonable amount and time, achieving an enhanced therapeutic effect and reduced side effects[36]. However, achieving drug delivery requires overcoming various barriers, including tumor penetration, cellular uptake by targeted cells, lysosome escape, and subcellular structure targeting[37]. Therefore, the ability of NPs to cross various biological barriers is the basis for judging the rational design of NPs, as well as being the key to their executive function.

Multicellular spheroids (MCSs) have been established to simulate tumor tissues, and have been widely used to investigate the penetration properties of nanotherapeutics into tumor tissues. As illustrated in Fig. 3A, 8 h after incubation of A549 cells with MCSs, the distributions of N770-DOX@NPs in MCSs exhibited significant differences in the presence or absence of NIR irradiation for 5 min. It was found that the penetration of NPs with NIR irradiation was much deeper than that of NPs without NIR irradiation, as clearly shown by the distribution of fluorescence signals of N770-DOX@NPs. This observation is due to the enhanced Brownian motion of NPs at a high temperature, which is induced by NIR irradiation. Furthermore, the quantitative data in Fig. 3B revealed that the red fluorescence intensity of the MCSs with NIR irradiation was about 1.3-fold stronger than that of the MCSs

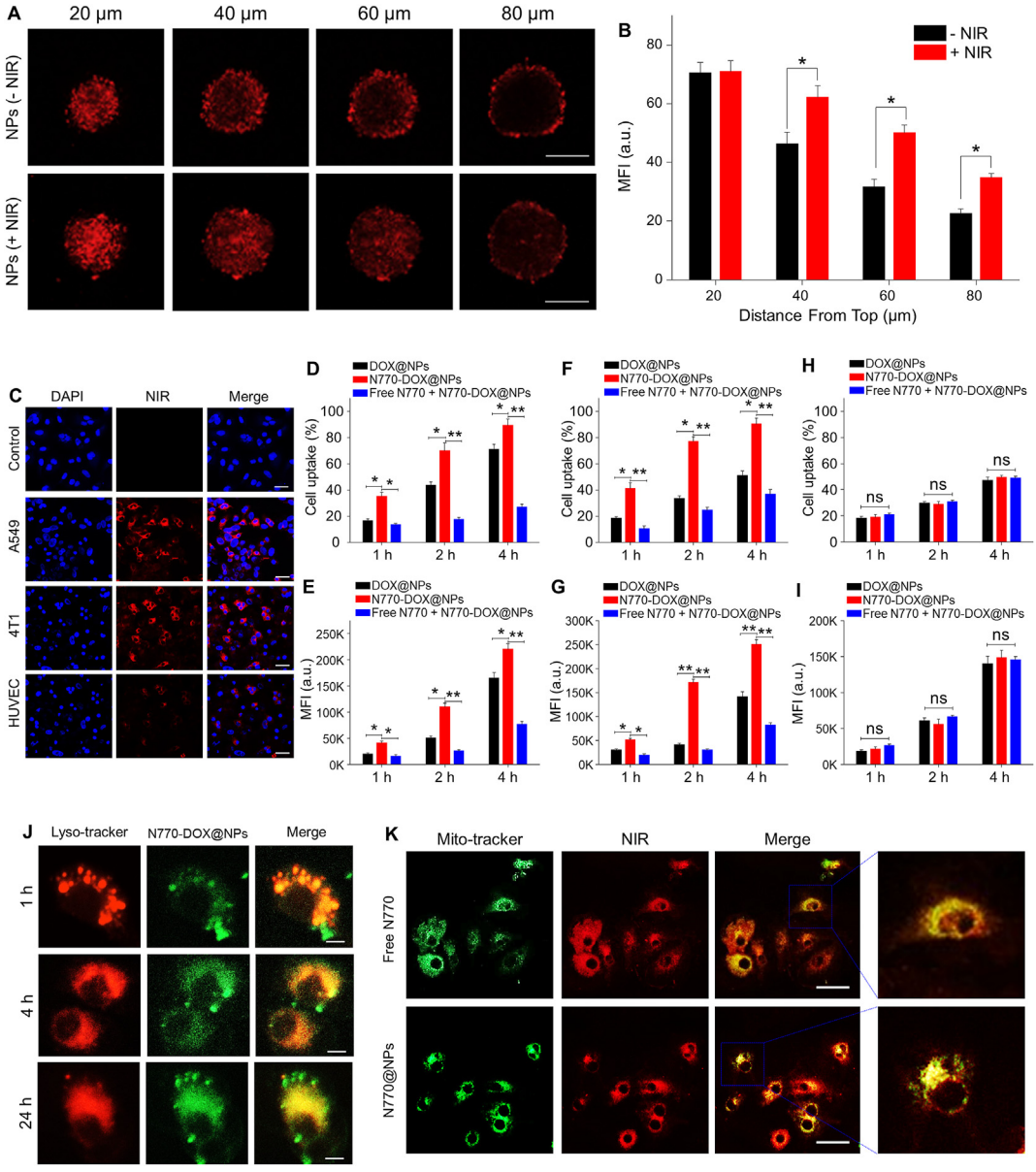

Figure 3 Internalization and intracellular distribution of NPs. (A) Penetration profiles and (B) the corresponding quantitative results (as mean fluorescence intensity, MFI) of N770-DOX@NPs in MCSs of A549 cells with or without NIR laser irradiation. Scale bars represent 100 μm. (C) Confocal images of cellular uptake profiles of N770-DOX@NPs in respective A549 cells, HUVECs, and 4T1 cells after incubation for 4 h. Nuclei were stained with DAPI (blue). Scale bar is 20 μm. (D) Percentages of DOX-containing A549 cells and (E) their corresponding MFIs after treatment with DOX@NPs, N770-DOX@NPs, and N770-DOX@NPs (+free N770) for 1, 2, and 4 h, respectively. (F) Percentages of DOX-containing 4T1 cells and (G) their corresponding MFIs after treatment with DOX@NPs, N770-DOX@NPs, and N770-DOX@NPs (+free N770) for 1, 2, and 4 h, respectively. (H) Percentages of DOX-contained HUVECs and (I) their corresponding MFIs after treatment with DOX@NPs, N770-DOX@NPs, and N770-DOX@NPs (+free N770) for 1, 2, and 4 h, respectively. These NP suspensions were prepared at equal DOX concentrations of 50 μg/mL. Data are expressed as mean ± SEM ($n = 3$; $^*P < 0.05$; $^*P < 0.01$; and ns = not significant). (J) Lysosomal escape properties of N770-DOX@NPs in A549 cells. Scale bar is 5 μm. (K) Mitochondrial co-localization profiles of N770-DOX@NPs in A549 cells. Scale bar is 20 μm.

without NIR irradiation. Furthermore, the penetrating results of N770-DOX@NPs in MCSs of 4T1 cells exhibited similar results to those above (Supporting Information Fig. S6). All these findings reveal that NIR irradiation can improve the penetration capacity of N770-DOX@NPs into MCSs.

Subsequently, the cellular uptake profiles and corresponding targeting capacities of N770-DOX@NPs were examined. Supporting Information Fig. S7 shows the determination by a CLSM of the cellular uptake of NPs by A549 cells at different time intervals. Obviously, higher fluorescence signals of NPs in cells were correlated with the treatment time, indicating that cellular uptake was time-dependent. Moreover, as shown in Fig. 3C, in comparison with normal cell lines (HUVEC), the tumor cell lines (A549 cells and 4T1 cells) exhibited a

significantly higher cellular uptake efficiency of the N770-DOX@NPs. FCM tests further revealed that the percentages of cellular uptake in tumor cell lines (A549 cells and 4T1 cells) treated with N770-DOX@NPs were significantly higher than those in tumor cell lines treated with DOX@NPs. Importantly, the addition of free N770 in the culture media significantly decreased the cellular uptake efficiency of N770-DOX@NPs (Fig. 3D−G). However, there were no obvious differences in cellular uptake efficiencies between DOX@NP-treated HUVECs and N770-DOX@NP-treated HUVECs (Fig. 3H and I). These results indicate that functionalizing the surface with N770 molecules could endow the NPs with tumor cell-targeting properties.

In order to clarify the mechanism of N770-mediated internalization, A549 cells were used as a model. Firstly, as presented in Supporting Information Fig. S8, a sharply decreased cellular uptake of N770-DOX@NPs was observed when the cells were incubated in an ice bath, indicating that the cellular uptake of NPs was energy-dependent. To investigate the possible uptake pathway, cells were pretreated with various endocytosis inhibition agents, including chlorpromazine (clathrin inhibitor), MβCD (caveolae inhibitor), and ciclosporin A [ATP-binding cassette (ABC) transporter inhibitor]. The results confirm that cellular uptake of NPs was dependent on molecule-mediated endocytosis instead of ABC transporter mechanism. Interestingly, when cancer cells were pretreated with BSP, a competitive inhibitor of OATP, the cellular uptake efficiency of N770-DOX@NPs was remarkably decreased. All these observations convincingly demonstrated that the targeting capacity of N770-functionalized NPs was achieved by an OATP-mediated endocytotic process.

A549 cells were incubated with N770-DOX@NPs at various time intervals, and then stained with lysosome-tracker to evaluate the capacity of N770-DOX@NPs to escape from the lysosome. As shown in Fig. 3J, with increasing incubation time, the coincidence of fluorescence by the lysosomes and NPs was greatly decreased, indicating the phenomenon of N770-DOX@NPs escaping the lysosomes. Furthermore, Pearson's Correlation Coefficient (PCC) was calculated using ImageJ software (National Institutes of Health, Bethesda, MD, USA) and used for quantitative analysis of the difference in fluorescence signal. The PCC value was 0.103 at the timepoint of 24 h, revealing that almost all the N770-DOX@NPs escaped from the lysosomes within 24 h, and suggesting the efficient escape of NPs from the endolysosomal compartment.

Localization of NPs in the mitochondria has been demonstrated to aggravate the degree of mitochondrial photodamage, which is expected to improve the phototherapeutic effect of N770-DOX@NPs. To confirm the mitochondrial localization of N770-DOX@NPs, A549 cells were stained with a mitochondrial tracker (Mito-tracker green). Fig. 3K shows that the red fluorescence signals (N770) overlapped well with the green fluorescence signals (mitochondria), suggesting that both free N770 and N770-DOX@NPs possessed excellent mitochondria-targeting capacity. In addition, the localization of mitochondria in 4T1 cell lines exhibited the same results as obtained with the A549 cells lines (Supporting Information Fig. S9). All these results demonstrate that N770 can facilitate accumulation in the mitochondria.

3.5. *In vitro synergistic therapy*

The ultimate goals of a rational design of nanotherapeutics are safety, efficiency, and improving clinical treatment procedures. Inspired by the multiple merits of N770-DOX@NPs mentioned above, they are speculated to have strong antitumor activities. The toxic effect on healthy cells is a critical concern for NDDSs. Thus, HUVEC, a normal cell line, was used to estimate the potential adverse toxicities of NPs. As shown in Supporting Information Fig. S10, free N770 and N770@NPs were observed to hardly be cytotoxic even at the N770 concentration of 200 μg/mL, suggesting their excellent biocompatibility.

Furthermore, MTT assay was also used to estimate the anticancer activities of N770-DOX@NPs against A549 cells and 4T1 cells, respectively. Twenty-four hours after co-incubation, free N770 showed negligible cytotoxicity against A549 cells (Fig. 4A) and 4T1 cells (Fig. 4B) even when its concentration was as high as 200 μg/mL, confirming the excellent biocompatibility of free N770. However, without NIR irradiation, DOX@NPs and N770-DOX@NPs exhibited obvious cytotoxicities against both A549 cells and 4T1 cells, and these cytotoxicities were concentration-dependent. DOX@NPs and N770-DOX@NPs without NIR irradiation were found to show much lower cytotoxicity against the normal cell line (HUVEC) than against tumor cell lines, which could be attributed to the low cellular uptake efficiency of NPs (Fig. 3H and I) and the low release rate of drugs from NPs due to the low ROS/GSH concentrations in healthy cells (Fig. 2B, C, E, and F). Moreover, we found that N770-DOX@NPs with NIR irradiation presented a stronger anti-cancer activity than free N770 (+NIR) and other treatment strategies, which could be due to their efficient cellular uptake and TME-responsive drug release capacities. These findings also confirmed the synergy between chemotherapy, PTT, and PDT. N770-DOX@NPs exhibited much higher cytotoxicities against tumor cells than DOX@NPs (Supporting Information Table S2), which was ascribed to the N770-mediated targeting capacity of N770-DOX@NPs.

To further verify whether the photo-induced PTT and PDT were synergistic against A549 cells, these cells were incubated with N770@NPs in an ice bath for PTT only or pretreated with *N*-acetylcysteine as an effective scavenger for PDT only, respectively. After treatment with NPs and/or NIR irradiation, cells were co-stained with calcein AM and PI, respectively. Fig. 4C indicates that the control cells were still alive, and the treatment with PTT only or PDT only resulted in extensive cell death. Strikingly, most A549 cells died upon combined treatment with PTT and PDT, indicating the synergy of PTT and PDT. An MTT assay was further conducted to confirm the synergy between PTT and PDT. Fig. 4D shows that the cell viabilities in all treatment groups decreased sharply within 24 h of treatment, and that the anti-tumor activity was N770 concentration-dependent. In particular, when the concentration of N770 reached 200 μg/mL, the PTT-only-treated group and the PDT-only-treated group had cell viabilities of 35.9% and 48.5%, respectively. Nevertheless, the cell viability in the cell group receiving combined treatment with PTT and PDT was 2.4%, confirming the synergistic effects of N770@NP (+NIR)-induced PTT and PDT.

Subsequently, the pro-apoptotic effects of various treatment strategies were determined by Annexin V-FITC/PI co-staining using FCM. Fig. 4E shows that the percentages of viable cells in the control group and the free N770 (−NIR)-treated group were 97.0%, revealing a negligible cytotoxicity in the dark. Treatment with free DOX only induced a low percentage of early apoptotic cells (21.3%). However, treatment with N770-DOX@NPs or free N770 (+NIR) resulted in large amounts of early apoptotic cells (around 70%) and small amounts of apoptotic cells. Interestingly, when A549 cells were incubated with N770-DOX@NPs (+NIR), the proportion of apoptotic cells was dramatically increased to

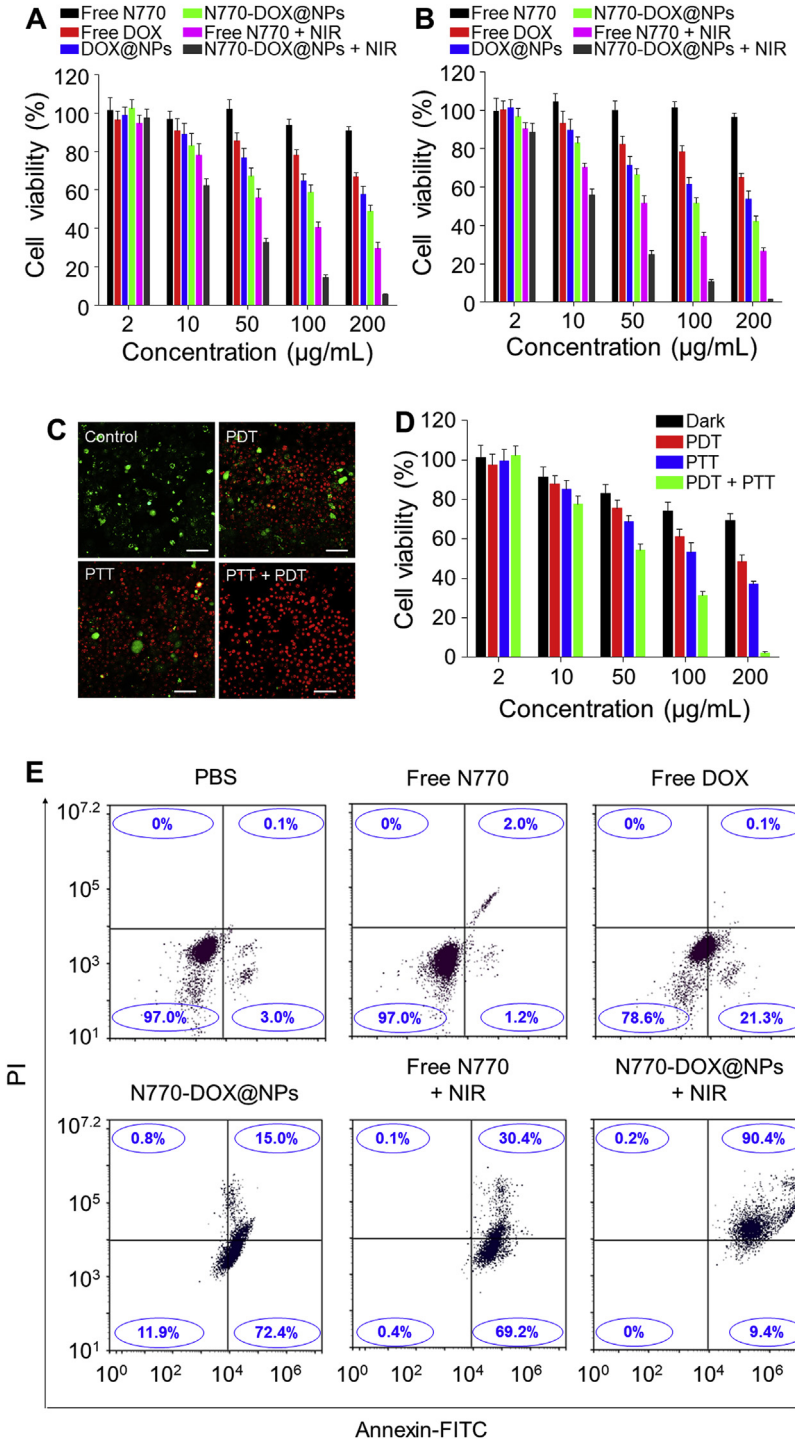

Figure 4 *In vitro* anti-cancer activity of NPs. Viabilities of (A) A549 cells and (B) 4T1 cells receiving different treatments. Data are expressed as mean ± SEM ($n = 5$). (C) Live/dead staining images and (D) viabilities of A549 cells after treatment for 24 h with PDT, PTT, or PDT/PTT simultaneously. Scale bar is 50 μm. Data are expressed as mean ± SEM ($n = 5$). (E) Apoptosis profiles of A549 cells receiving various treatments. Data are expressed as mean ± SEM ($n = 3$).

90.4%, which was much higher than that in the other treatment groups. We also found that the pro-apoptotic capacity of the N770-DOX@NPs (+NIR) against A549 cells exhibited concentration dependence (Supporting Information Fig. S11). Moreover, the corresponding assay of live and dead cells co-stained with calcein AM and PI (Fig. 5A) confirmed these results.

To investigate the pro-apoptotic mechanism of NPs, the variations in the mitochondrial membrane potential, intracellular ROS generation, and apoptosis protein expression profiles were determined. A decrease of the mitochondrial membrane potential has been recognized as an important sign of cell apoptosis. When the potential of the mitochondrial membrane was normal, the JC-1

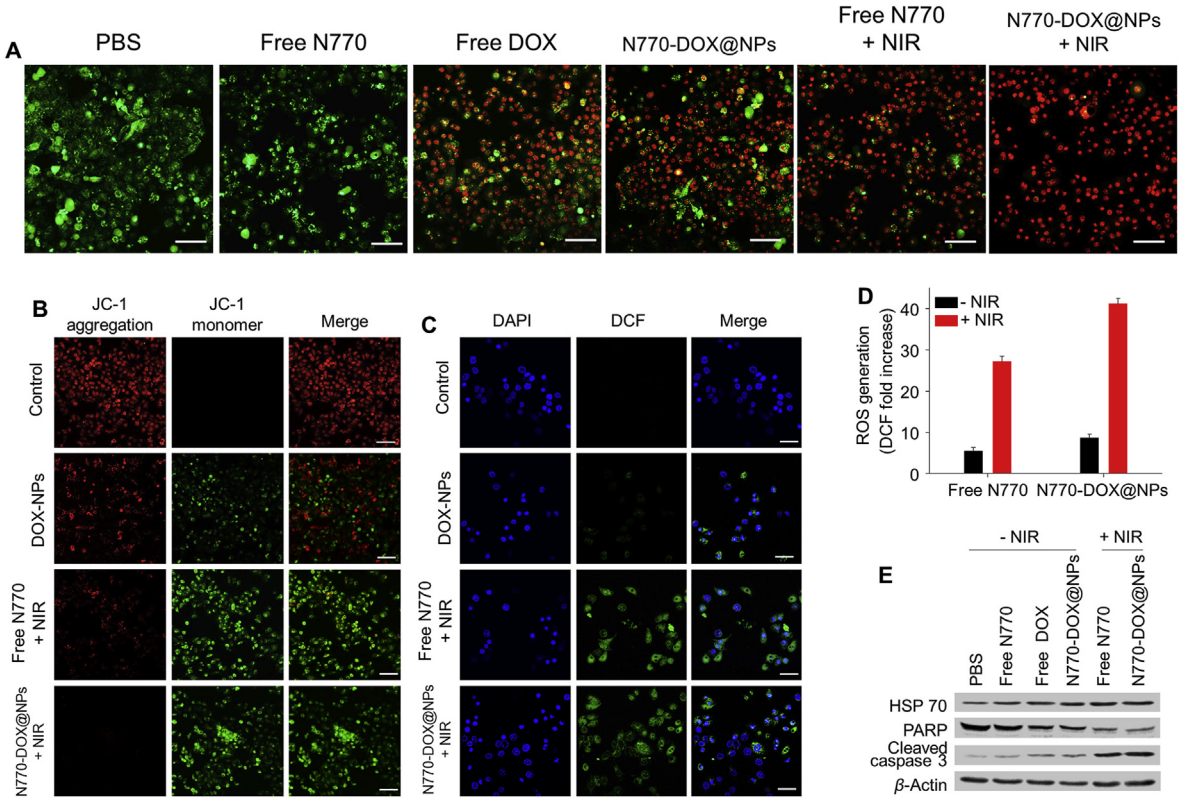

Figure 5 (A) Live/dead staining images of A549 cells receiving various treatments. Scale bar is 50 μm. (B) Mitochondrial damage analysis of A549 cells treated with DOX@NPs, free N770 (+NIR), and N770-DOX@NPs (+NIR), and further stained with JC-1 fluorescent probes. Scale bar is 50 μm. (C) Confocal images of intracellular ROS generation profiles of A549 cells treated with DOX@NPs, free N770 (+NIR), and N770-DOX@NPs (+NIR), and further stained with DCFH-DA fluorescent probes. Nuclei were stained with DAPI (blue). Scale bar is 20 μm. (D) Relative quantification of the amounts of ROS generated in A549 cells after treatment with free N770 solution and N770-DOX@NP suspension with or without NIR irradiation. Data are expressed as mean ± SEM ($n = 3$). (E) Western blots to determine the expression levels of heat shock protein (HSP70) and apoptosis-related proteins (PARP and cleaved caspase-3) in A549 cells receiving various treatments.

probe tended to aggregate in the mitochondrial matrix and display red fluorescence. However, when the membrane potential decreased, the JC-1 probe would remain as a monomer and emit green fluorescence. Thus, the JC-1 probe was applied to evaluate variations of the mitochondrial membrane potential of A549 cells receiving various treatments. As shown in Fig. 5B, the control group exhibited a normal mitochondrial membrane potential as demonstrated by the emission of red fluorescence. The DOX@NP-treated cells exhibited both red fluorescence and green fluorescence, indicating that part of the A549 cells presented apoptotic signs. Interestingly, almost all the cells in the groups treated with free N770 (+NIR) and N770-DOX@NP emitted green fluorescence, suggesting the sharp decrease of the mitochondrial membrane potential upon NIR irradiation. Additionally, we found that the profiles of decreasing mitochondrial membrane potential of N770-DOX@NP (+NIR)-treated A549 cells was concentration-dependent (Supporting Information Fig. S12).

ROS are known to be a major cause of PDT-induced apoptosis, and DCFH-DA fluorescent probe was used to determine the intracellular amounts of ROS. A549 cells were incubated with different samples for 24 h, and treated with DCFH-DA probe to detect the generated ROS. Fig. 5C indicates that no green fluorescence signal was detected in the control cells, while the DOX@NP-, free N770 (+NIR)-, and N770-DOX@NP (+NIR)-treated groups showed clear green fluorescence. Furthermore, we found that NIR treatment increased the generated amounts of ROS in the free N770- and N770-DOX@NP-treated groups. Specifically, the amount of ROS in the group receiving treatment with N770-DOX@NPs (+NIR) was 5.0-fold more than that in the N770-DOX@NP (−NIR)-treated group (Fig. 5D), suggesting a synergistic effect of N770 and DOX in ROS generation. The N770-DOX@NP (+NIR)-treated group demonstrated the strongest ROS generation capacity among all the treatment groups, and the amount of ROS generated in this group was approximately 1.5-fold higher than that in the group with the treatment of free N770 (+NIR). In addition, it was found that the ROS generation profiles of the N770-DOX@NP (+NIR)-treated group was dependent on the N770 concentration (Supporting Information Fig. S13).

To discover the potential mechanism of N770-DOX@NP-mediated synergistic cancer therapy, the expression profiles of apoptosis-related proteins were evaluated by Western blotting. As seen in Fig. 5E, comparable expression levels of cleaved caspase-3 and poly ADP-ribose polymerase (PARP) were found in the N770-DOX@NP-treated cells and the PBS control group. However, when A549 cells were treated with free N770 (+NIR) and N770-DOX@NPs (+NIR), the expression of cleaved caspase-3 increased sharply, while the expression of *PARP* was remarkably

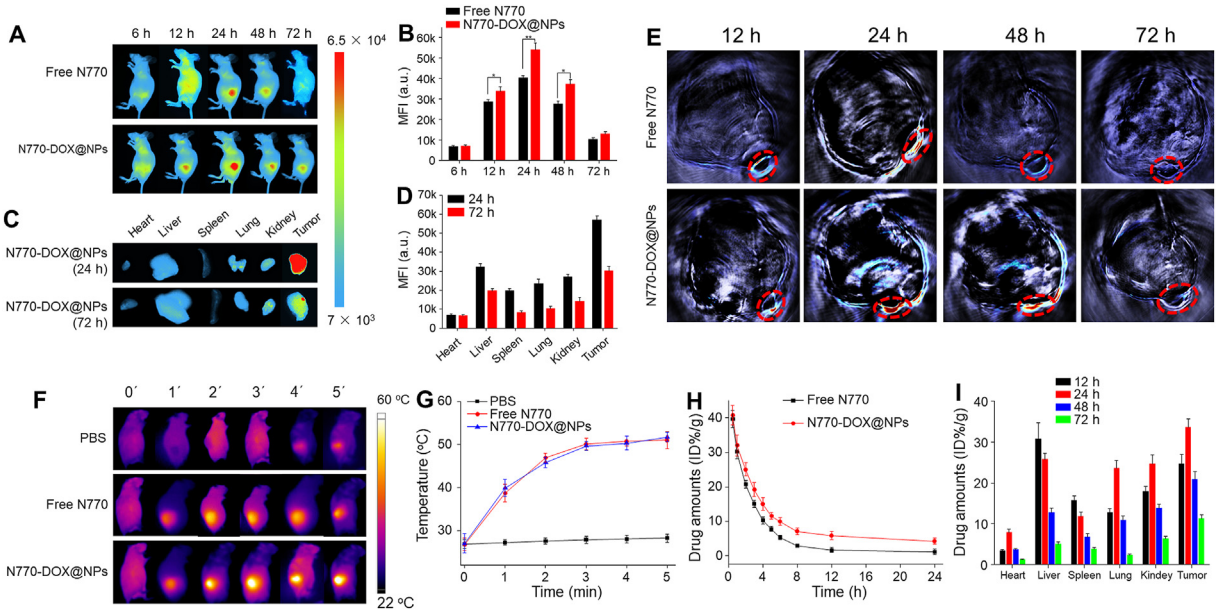

Figure 6 *In vivo* bio-distribution of NPs in mice bearing A549 lung carcinoma xenografts. (A) FLI of mice bearing A549 tumor after intravenous injection of free N770 solution and N770-DOX@NP suspension at an equal N770 concentration of 1 mg/kg (B) MFIs of tumor tissues from mice after treatment with free N770 and N770-DOX@NPs at different timepoints (6, 12, 24, 48, and 72 h). Data are expressed as mean ± SEM ($n = 3$; $^*P < 0.05$; $^{**}P < 0.01$; and ns = not significant). (C) *Ex vivo* FLI and (D) corresponding quantitative data of fluorescence intensities in the five major organs and tumor tissues from mice after the treatment with N770-DOX@NPs (N770: 1 mg/kg) at the timepoints of 24 and 72 h. Data are expressed as mean ± SEM ($n = 3$; $^*P < 0.05$; $^{**}P < 0.01$; and ns = not significant). (E) PAI of tumor tissues from mice after treatment with free N770 and N770-DOX@NPs at different timepoints (12, 24, 48, and 72 h). (F) PTI of mice bearing A549 tumor after intravenous injection of free N770 solution and N770-DOX@NP suspension at an equal N770 concentration of 1 mg/kg for 24 h upon 808 nm laser irradiation (0.8 W/cm^2, 5 min), and (G) temperature profiles of tumors monitored by infrared thermal camera. Data are expressed as mean ± SEM ($n = 3$). (H) Variation of N770 concentrations in serum after intravenous injection of free N770 solution and N770-DOX@NP suspension at an equal N770 concentration of 1 mg/kg. Data are expressed as mean ± SEM ($n = 3$). (I) Quantification of drug amounts in the major organs and tumor tissues at different timepoints *post* injection (12, 24, 48, and 72 h). Data are expressed as mean ± SEM ($n = 3$).

decreased. These findings clearly revealed that the anti-cancer activity of N770-DOX@NPs (+NIR) was induced by the caspase-dependent apoptosis pathway.

Collectively, the above results demonstrate that the enhanced anti-tumor activity of N770-DOX@NPs upon NIR irradiation can be attributed to the N770-mediated dual-level targeting (cancer cell and mitochondria), the response to multiple stimuli, and the synergy of chemotherapy, PTT, and PDT.

3.6. *In vivo bio-distribution*

The *in vivo* distribution of NDDSs plays an important role in their tumor diagnosis and tumoricidal efficacy. Thus, murine lines carrying A549 lung carcinoma xenografts or 4T1 breast carcinoma xenografts were established to assess the *in vivo* bio-distribution of N770-DOX@NPs. Initially, mice from these two models were injected with free N770 solution or N770-DOX@NP suspension *via* the tail vein, and FLI was carried out at different timepoints (6, 12, 24, 48, and 72 h). As shown in Fig. 6A, faint N770 fluorescence signals were detected after intravenous administration of free N770 solution and N770-DOX@NP suspension at 6 h, indicating that they began to enrich in A549 lung tumor tissues at this timepoint. The maximal NIR fluorescence signals in tumor tissues were observed at the 24-h timepoint for both the free N770-treated group and the N770-DOX@NP-treated group. Moreover, the fluorescence signals of N770-DOX@NPs were still clearly distinguishable even 72 h after injection. The further quantitative results revealed that the fluorescence intensity of tumor sites in the N770-DOX@NP-treated group was significantly higher than that in the free N770-treated group (Fig. 6B), suggesting the preferential enrichment of N770-DOX@NPs in A549 lung tumor tissues. In addition, we found similar accumulation and retention of N770 in tumor tissues in the mouse model carrying a 4T1 breast carcinoma xenograft (Supporting Information Fig. S14A and B).

To verify the aforementioned observations by *in vivo* mouse imaging, the five major organs and A549 lung tumor tissues were harvested, and imaged at the timepoints of 24 and 72 h, respectively. It was found that the NIR fluorescence signals in all these organs and tissues were weakened as time extended (Fig. 6C). Notably, tumor tissues showed the highest N770 fluorescence intensities among all the organs and tissues (Fig. 6D). Nevertheless, *ex vivo* imaging of the major organs and tumors from mice of the 4T1 breast tumor-bearing mouse model also demonstrated the preferential long-term retention of N770-DOX@NPs in tumor tissues (Fig. S14C and D). Inspired by the superior photothermal conversion efficiency of N770-DOX@NPs, their photoacoustic (PA) signal production profile was evaluated. Fig. 6E revealed that the PA intensity of A549 lung tumor tissues gradually amplified over time, reaching a plateau at the timepoint of 24 h. We also found that at this timepoint, tumor tissues from the group receiving treatment with N770-DOX@NPs showed much stronger PA signals than those from the group treated with free N770. As expected, the time-dependence of PA intensities in the tumor sites was strictly coincident with the FLI results. Thus, N770-

DOX@NPs with FLI and PAI properties hold a great potential for precise tumor diagnosis and multi-model imaging-guided treatment.

To confirm the *in vivo* light-to-thermal conversion performance of N770-DOX@NPs, their photothermal effects were monitored at 24 h post injection upon NIR laser irradiation using an infrared thermal camera. As observed in Fig. 6F, the temperature of the A549 xenograft tumors from the control group slightly increased to 28.7 °C after 5 min NIR irradiation. In sharp contrast, temperature in the A549 xenograft tumors from free N770- and N770-DOX@NP-treated groups drastically increased to around 51.6 °C at the end of NIR irradiation, which was expected to be high enough to damage tumor tissues (Fig. 6G). Additionally, the temperature variation in the mouse model bearing 4T1 breast xenograft tumors exhibited a similar trend as that in the A549 lung tumor xenograft mouse model (Fig. S14E and F). The tumor-specific accumulation and phototherapeutic effect of N770-DOX@NPs potentially avoid damage to healthy tissues.

Furthermore, the pharmacokinetic profiles of free N770 and N770-DOX@NPs were compared in BALB/c mice. In this study, mice were divided into three groups, namely the control group, the free N770-treated group (N770, 3 mg/kg), and the N770-DOX@NP-treated group (N770, 3 mg/kg). The fluorescence intensities of N770 in blood were quantified to analyze the pharmacokinetic properties. The N770 concentration *versus* time curve is shown in Fig. 6H. It indicated that free N770 had a much shorter circulatory half-life than N770-DOX@NPs, suggesting that N770-DOX@NPs could greatly prolong the circulation time of N770 in the blood. We also found that the circulatory half-life of N770 in N770-DOX@NPs was longer than that of DOX (Supporting Information Fig. S15), revealing that the chemical conjugation (N770) to the NPs could prolong the circulation time compared with the physical encapsulation approach (DOX). Meanwhile, the fluorescence intensities of N770 and the amounts of DOX in different organs and tumor tissues implied that the amounts of N770-DOX@NPs in tumor tissues were drastically decreased 24 h after administration (Fig. 6I). Much more DOX was accumulated in the tumor tissues from mice receiving the treatment of N770-DOX@NPs, in comparison with that of DOX@NPs (Figs. S16 and S17). It is worth noting that the decrease rate of N770 fluorescence intensity in the liver was faster than that in tumor tissue, which could be due to the canalicular export and basolateral uptake in the liver.

Overall, we demonstrate that N770-DOX@NPs have the capacity to efficiently accumulate in tumor tissues and are retained there a relatively long time, which can be attributed to the passive tumor-homing of NPs based on the enhanced permeability and retention (EPR) effect and N770-mediated active tumor targeting.

3.7. *In vivo anti-tumor outcomes*

To evaluate the anti-cancer effects of various treatment strategies, three tumor models were established, including an A549 lung tumor xenograft mouse model, a 4T1 breast tumor xenograft mouse model, and a lung cancer PDX mouse model. Initially, the tumoricidal activities of the nanotherapeutics were evaluated using the A549 lung tumor xenograft mouse model. These mice were intravenously injected with free drugs or NPs at a N770 amount of 2.13 mg/kg and/or a DOX amount of 3 mg/kg on Days 0 and 3. Twenty-four hours after intravenous injection, groups with N770 in the treatment were exposed to 808 nm laser irradiation (0.8 W/cm^2, 5 min).

A schematic illustration of the experimental procedure is presented in Fig. 7A. No significant body weight variations were detected in any of the treatment groups compared with the PBS control group (Fig. 7B), suggesting the relative safety of these treatment strategies. Fig. 7C presents the variations of tumor volumes. It was obvious that the tumor volumes increased rapidly in the PBS control group throughout the entire investigation, and that the treatment with PBS (+NIR) or free N770 could not retard tumor growth, indicating that NIR irradiation alone or free N770 administration alone had no retarding effect. However, the tumor growth rates were obviously decreased to various extents in the mouse groups receiving other treatment strategies when compared with the PBS control group. Furthermore, it was found that the tumor inhibition rate of DOX@NPs was comparable to that of N770-DOX@NPs, and was significantly higher than that of free DOX. These findings indicate that these NPs can remarkably increase the therapeutic effect of free DOX against lung tumor. Strikingly, we found that tumor volumes in the N770-DOX@NP-treated group were significantly larger than those in the N770-DOX@NP (+NIR)-treated group, suggesting the synergistic anti-tumor effects of chemotherapy and phototherapy. It is worth noting that of all treatment groups, the treatment with N770-DOX@NPs (+NIR) exhibited the best anti-tumor effect; there were almost no tumor tissues in this treatment group at the end of the investigation (Fig. 7D and E). Although the DOX@NP-treated group showed a tumor volume comparable to that of the N770-DOX@NP-treated group, the former group had much heavier tumors than the latter (Fig. 7F). It should be noted that tumor sizes and weights were measured by vernier calipers and an electronic balance, respectively, which give semi-quantitative and quantitative results, respectively. Therefore, the tumor weight results were more reliable than the tumor size data. Additionally, we found that the tumor inhibition ratio (Fig. 7G) confirmed the effective treatment efficacy of N770-DOX@NPs plus NIR irradiation.

Subsequently, the tumor ablation profiles were evaluated by magnetic resonance imaging (MRI). Obviously, the PBS control group, the free DOX-treated group, the free N770-treated group, and the N770-DOX@NP-treated group displayed distinct tumor tissues (Fig. 7H). On the contrary, no detectable tumor tissues were found in the N770-DOX@NP (+NIR)-treated group. Moreover, angiography was employed to determine the capillary networks in the various treatment groups. It was found that a capillary network was abundantly present in tumor tissues from the PBS control group and the free DOX-treated group. In the N770-DOX@NP-treated group, the capillary networks were much looser than in the PBS control group. Interestingly, very few capillary signals were detected in the N770-DOX@NP (+NIR)-treated group, revealing that the combined application of chemotherapy and phototherapy could effectively eliminate the capillary networks in tumor tissues.

NIR irradiation-mediated ROS generation is one of the main reasons that tumor cells are killed in phototherapy[38]. To confirm this point, frozen sections of tumor tissues were stained with ROS fluorescence probe (SOSG fluorescence probe). As shown in Supporting Information Fig. S18, no obvious ROS signal was found in the tumor tissues from the PBS groups with or without NIR irradiation. We further found that the tumor sections from the N770-DOX@NP (+NIR) group generated the highest amount of ROS among all treatment groups, demonstrating the efficient

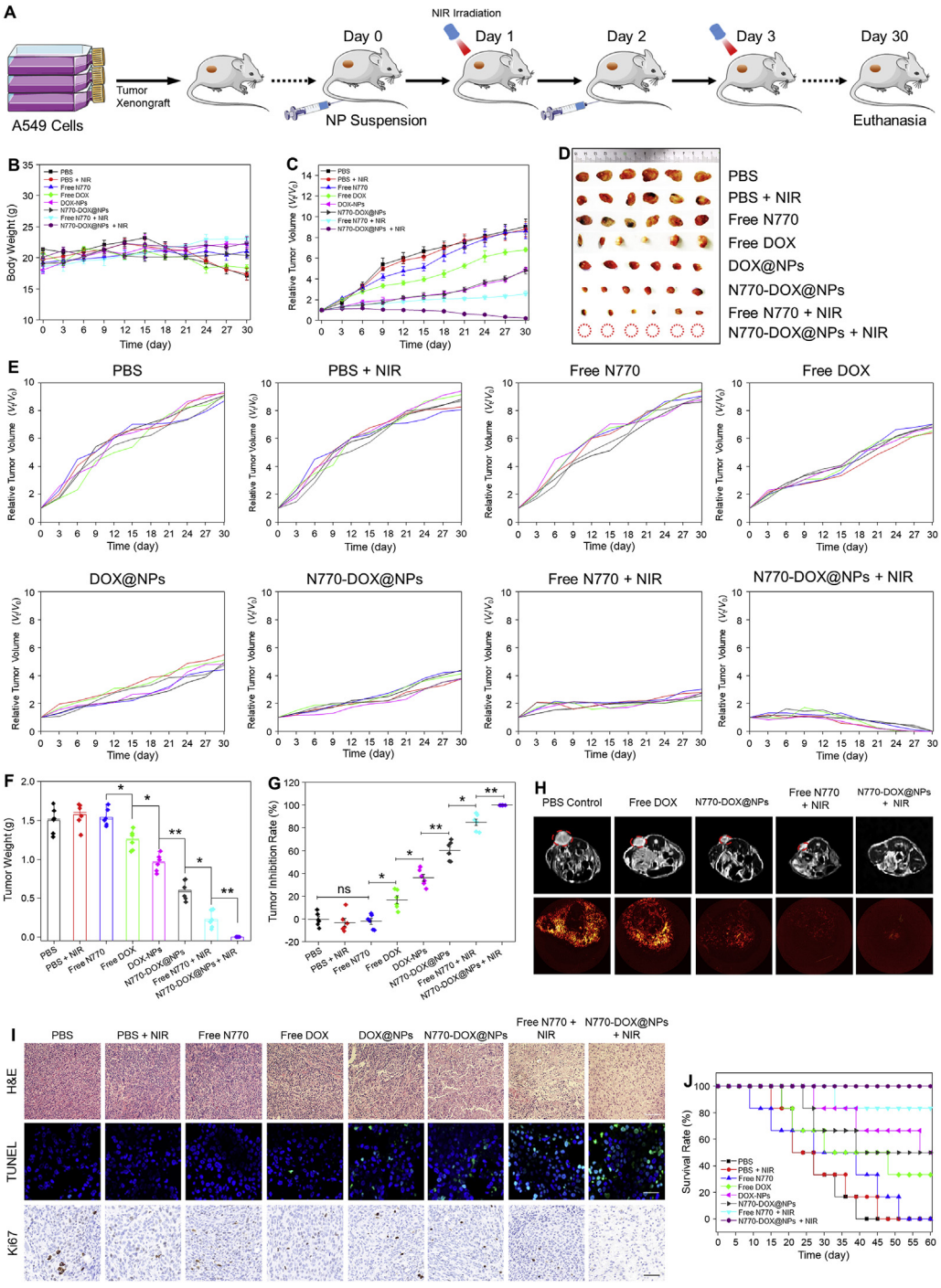

Figure 7 *In vivo* anti-cancer outcomes of NPs based on the A549 lung tumor xenograft mouse model. (A) Schematic illustration of the treatment processes. (B) Body weight changes and (C) tumor growth curves of mice bearing A549 lung carcinoma xenografts. Data are expressed as mean ± SEM ($n = 6$). (D) Photographic images of tumors from various treatment groups at the end of experiments. (E) Individual tumor growth profiles of mice from the various treatment groups. (F) Tumor weights and (G) tumor inhibition rates of mice from the various treatment groups. Data are expressed as mean ± SEM ($n = 6$; $^*P < 0.05$; $^{**}P < 0.01$; and ns = not significant). (H) Detection of tumor tissues and tumor vascularity from various treatment groups at the end of experiments using MRI and angiography, respectively. (I) H&E staining, TUNEL staining, and Ki67 staining of tumor sections from different treatment groups. Scale bar represents 50 μm. (J) Survival rates for the different treatment groups (six mice in each group). The median survival time of each group was labeled above each curve.

generation of ROS in tumor tissues from mice in the group receiving treatment with N770-DOX@NPs plus NIR irradiation.

TME is known to be hypoxic, which is not favorable for PDT. To evaluate the impact of different treatment approaches on the hypoxic condition in TME, tumor tissue sections were assessed by immunofluorescence assay. Supporting Information Fig. S19 shows that the PBS control group and the PBS (+NIR) group had high expression levels of hypoxia inducible factor-α (HIF-α).

By contrast, the treatment with N770-DOX@NPs or N770-DOX@NPs (+NIR) significantly decreased the HIF-α expression levels in tumor tissues. Remarkably, there was no clear HIF-α signal in the tumor tissue sections from the N770-DOX@NP (+NIR) group. These results suggest that the treatment with N770-DOX@NPs plus NIR irradiation can effectively alleviate the hypoxic condition of tumor tissues, thus enhancing the PDT effect of N770.

H&E staining was applied to evaluate the pathological changes of tumor tissues from different treatment groups. As presented in Fig. 7I, the N770-DOX@NP (+NIR) group showed extensive destruction of the tumor tissues with the least number of tumor cells when compared to the PBS control group and other treatment groups with abundant and densely arranged tumor cells. Thereafter, TUNEL assay and Ki67 staining assay were used to assess the apoptosis and proliferation profiles of tumor tissues, respectively. It was obvious that very few TUNEL signals but clear Ki67 signals were detected in the tumor tissues from the PBS control group, the PBS-treated group plus NIR irradiation, and the free N770-treated group, indicating the exuberant division and proliferation capacity of tumor cells in these experimental groups. On the contrary, distinct TUNEL signals were detected in other treatment groups. In particular, the tumor tissues from the N770-DOX@NP (+NIR) group exhibited the most apoptotic cells and the least Ki67-positive cells among all the mouse groups. Importantly, the survival rates of the experimental groups receiving PBS, PBS (+NIR), free N770, free DOX, DOX@NPs, N770-DOX@NPs, free N770 (+NIR), and N770-DOX@NPs (+NIR) were 0%, 0%, 0%, 33.3%, 50%, 50%, 83.3%, and 100%, respectively (Fig. 7J). The longest lifespan of the N770-DOX@NP (+NIR) group confirmed that the therapeutic effect of N770-DOX@NPs plus NIR irradiation against lung tumors was best, which could be attributable to the NP's tumor-targeting capacity and TME-specific drug release, and the synergistic anti-tumor effects of phototherapy and chemotherapy.

Considering the excellent *in vitro* targeting properties and anti-tumor activities of N770-DOX@NPs in both A549 and 4T1 cells, a 4T1 breast cancer xenograft mouse model was established to confirm their broad *in vivo* anti-tumor property (Supporting Information Fig. S20A). As seen in Fig. S20B, the PBS control group, the PBS-treated group plus NIR irradiation, and the free N770-treated group showed clear decreases in body weight at the end of the experiment. However, other treatment groups maintained a stability in body weight after the treatments, indicating that the groups receiving the treatment involving DOX- and/or N770 (+NIR) could effectively retard the trend of decreasing body weight. Variations of the tumor volumes in different treatment groups were highly consistent with those in the A549 lung cancer xenograft mouse model. Specifically, treatment with N770-DOX@NPs (+NIR) presented the best anti-breast cancer effects among all the treatment groups, which was confirmed by the variations in tumor volume (Fig. S20C), by tumor photography (Fig. S20D), individual tumor growth curves (Fig. S20E), tumor weights (Supporting Information Fig. S21A), and tumor inhibition rates (Fig. S21B). Moreover, we found that lung metastases of breast cancer were significantly inhibited by the different treatment approaches. As shown in Supporting Information Figs. S22 and S23, 15 metastatic nodules were observed in the lung from the PBS control group, and this number was significantly reduced after treatment involving N770 and/or DOX. The H&E, TUNEL and Ki67 staining results further revealed that the treatment with N770-DOX@NPs plus NIR irradiation could effectively kill the tumor cells through the induction of apoptosis and by decreasing their ability to proliferate (Supporting Information Fig. S24). In addition, the therapeutic effects of N770-DOX@NPs plus NIR irradiation were verified by the lifespan of mice in the group receiving this treatment being the longest (Supporting Information Fig. S25).

To further illustrate the potential for clinical utility, cancer specimens derived from patients with lung carcinoma were collected. These specimens were implanted subcutaneously on the left side of normal nude mouse to establish a PDX mouse model (Fig. 8A). The obtained PDX mice were divided into six groups, namely the PBS control group, the PBS (+NIR)-treated group, the free N770-treated group, the N770-DOX@NP-treated group, the free N770 (+NIR) group, and the N770-DOX@NP (+NIR) group. To determine the tumor accumulation properties of the therapeutics in this PDX mouse model, free N770 or N770-DOX@NPs were intravenously injected and *in vivo* FLI was performed at the timepoints of 12, 24, 48, and 72 h post administration. Obviously, the strongest fluorescence intensities were observed in the tumor site at 24 h post injection for both free N770- and N770-DOX@NP-treated groups (Fig. 8B). We also found that at this timepoint, the N770-DOX@NP-treated group showed much stronger fluorescence intensities than the group with the treatment of free N770, suggesting the preferential accumulation of N770-DOX@NPs in tumor tissues (Fig. 8C). Twenty-four hours after administration of free N770 and N770-DOX@NPs, the PDX mice were given an NIR laser irradiation at the tumor-transplanted site. It was obvious that the temperature of tumor tissues could increase to around 50 °C within 5 min (Fig. 8D and E), indicating the effective photothermal effect in PDX mouse model. Mice received various treatments at amounts of N770 of 2.13 mg/kg on Days 0 and 3. Tumor tissues from the groups with NIR involved were exposed to 808 nm laser irradiation (0.8 W/cm^2) for 5 min at 24 h after each injection. As presented in Fig. 8F, the body weight change profiles of the PDX model receiving different treatments were consistent with those of the above two mouse models. Significant differences in tumor volume were found between the various treatment groups. As shown in Fig. 8G the best tumor inhibition rate was achieved by the treatment with N770-DOX@NPs plus NIR irradiation. Photography of the excised tumors further confirmed that N770-DOX@NPs plus NIR irradiation possessed a strong capacity to eliminate the subcutaneous tumor tissues from the PDX mouse model (Fig. 8H−K). At the end of the experiment, tumor specimens were retrieved and H&E, TUNEL, and Ki67 assays were performed. Apoptosis of tumor cells was clearly detected in the tumor tissues from the PDX mouse group treated with N770-DOX@NPs plus NIR irradiation (Fig. 8L), confirming the excellent therapeutic outcomes of N770-DOX@NPs against PDX tumors upon NIR irradiation. Besides, histological examinations of the five major organs from the various mouse groups showed no obvious tissue damage (Supporting Information Fig. S26).

3.8. *In vivo biosafety*

Last, we evaluated the biosafety of N770-DOX@NPs, as this property is a critical parameter for the medical implementation of nanotherapeutics to cancer therapy. Initially, we evaluated the hemocompatibility of N770-DOX@NPs. Supporting Information Fig. S27A revealed that no obvious hemolytic phenomenon was observed when the N770 concentration was as high as 20 μmol/L.

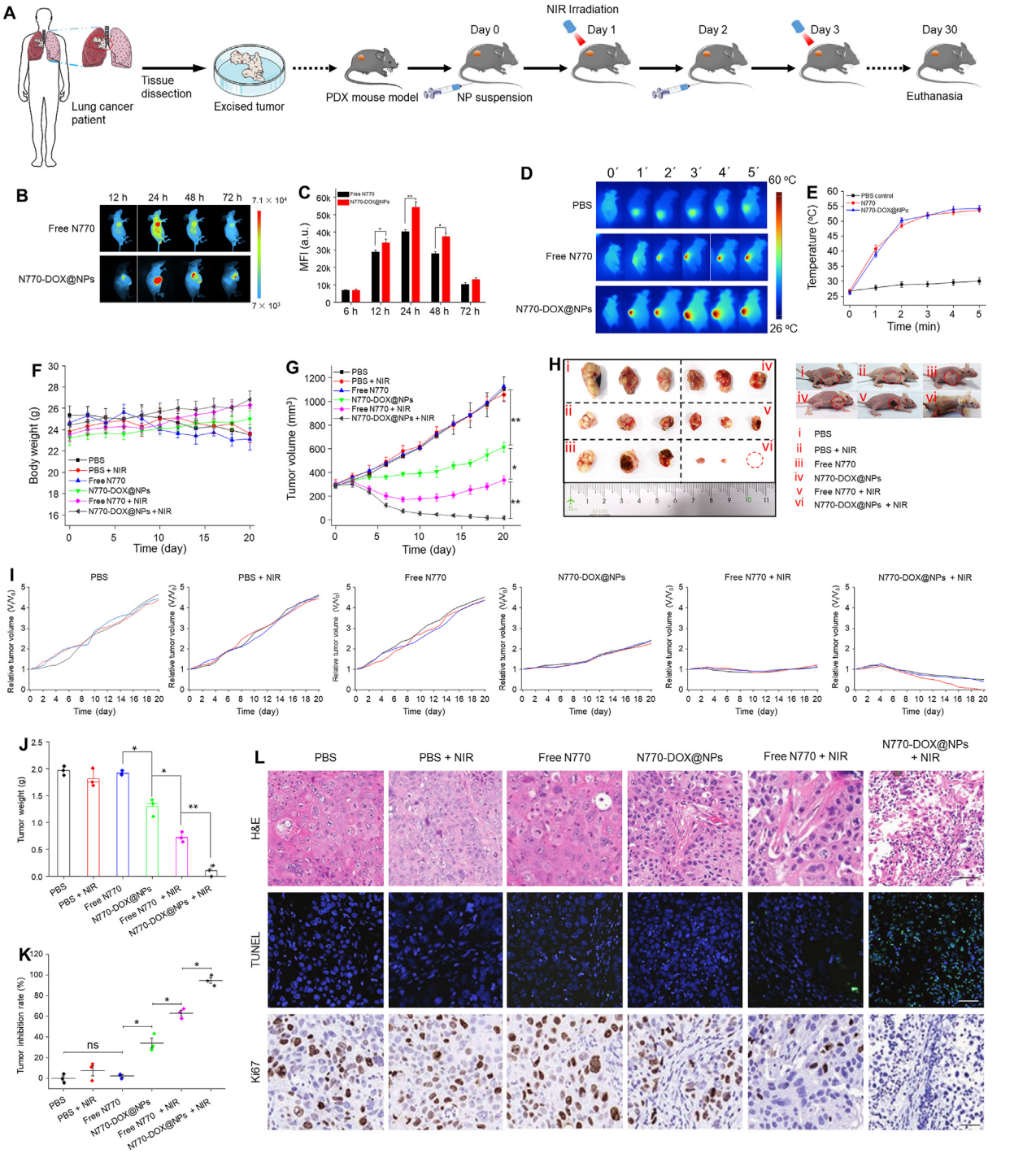

Figure 8 *In vivo* anti-cancer outcomes of NPs in a lung cancer PDX mouse model. (A) Schematic illustration of the treatment processes. (B) FLI of mice bearing A549 tumor after intravenous injection of free N770 solution and N770-DOX@NP suspension at an equal N770 concentration of 1 mg/kg. (C) MFIs of tumor tissues from mice after the treatment with free N770 and N770-DOX@NPs at different timepoints. Data are expressed as mean ± SEM ($n = 3$; $^{*}P < 0.05$; $^{**}P < 0.01$; and ns = not significant). (D) PTI of PDX mice after intravenous injection of free N770 solution and N770-DOX@NP suspension at equal N770 concentrations of 1 mg/kg for 24 h upon 808 nm laser irradiation (0.8 W/cm^2, 5 min), and (E) the temperature profiles of PDX tumors monitored by infrared thermal camera. Data are expressed as mean ± SEM ($n = 3$). (F) Body weight changes and (G) tumor growth curves of PDX mice. Data are expressed as mean ± SEM ($n = 3$). (H) Photographic images of tumors from various treatment groups at the end of experiments. (I) Individual tumor growth profiles of mice in the various treatment groups. (J) Tumor weights and (K) tumor inhibition rates of mice in the various treatment groups. Data are expressed as mean ± SEM ($n = 3$; $^{*}P < 0.05$; $^{**}P < 0.01$; and ns = not significant). (L) H&E staining, TUNEL staining, and Ki67 staining of tumor sections from different treatment groups. Scale bar represents 50 μm.

Furthermore, the resulting hemoglobin concentrations indicated the extremely low hemolysis of N770-DOX@NPs, in comparison with the positive control group (Fig. S27B). Next, the *in vivo* hemolytic evaluation further confirmed that the blood routine of mice hardly changed after administration of N770-DOX@NPs. In addition, all tested blood factors such as white blood cells (WBC), red blood cells (RBC), hemoglobin (HGB), mean cell hemoglobin (MCH), mean corpuscular hemoglobin concentration (MCHC), and platelets (PLT), were in the normal ranges, suggesting the excellent compatibility of N770-DOX@NPs with blood (Fig. S27C).

In addition, the long-term adverse effects of these therapeutics were evaluated. BALB/c mice were divided into four groups, namely a PBS control group, a free N770-treated group, a blank NP-treated group, and a N770-DOX@NP-treated group. Body weights of mice from all the groups were recorded during the entire experiment (Supporting Information Fig. S28A). All the mouse groups showed a slight weight increase, and the organ indices of the five major organs from all the treatment groups showed no significant variations compared with those of the PBS control group (Fig. S28B). Moreover, mouse whole blood and serum were gathered at different timepoints (1, 5, 10, and 20 days) to evaluate the blood routine and analysis of the bio-active molecules. The results of the complete blood count show no significant differences among all the mouse groups in the tested parameters (Fig. S28C and S28D). The potential side effects of NPs against the liver and spleen were evaluated, as part of these NPs was distributed in these two organs. Alkaline phosphatase (ALP), alanine aminotransferase (ALT), and aspartate aminotransferase (AST) are the serological indexes of liver function (Supporting Information Fig. S29). Compared with the PBS control group, none of the treatment groups displayed any variations in these three serological indexes. Additionally, blood urea nitrogen (BUN) and creatinine (CREA), parameters reflecting kidney function, displayed no distinct differences in any of the groups. Moreover, histological analysis (H&E staining) of the main organs (heart, liver, spleen, lung, and kidney) showed negligible damage in all the treatment groups (Supporting Information Fig. S30). Therefore, the above results demonstrate that N770-DOX@NPs have a perfect safety performance after intravenous administration.

4. Conclusions

In this investigation, we produced a N770-coated DOX-loaded nanoplatform targeted at the mitochondria of tumor cells, releasing the drug in response to four different stimuli, allowing trimodal imaging, and with synergistic PTT/PDT/chemotherapeutic effects. These nanoplatforms (N770-DOX@NPs) showed distinct capacities in response to pH/ROS/GSH/hyperthermia because of the presence of β-sheet regions and disulfide linkages, achieving controlled drug release in tumor cells. They can be specifically internalized by tumor cells and be further retained in mitochondria, which would be favorable for visualizing the tumor margins, mitochondrial phototherapy guided by imaging, and targeted chemotherapy. We also found that N770-DOX@NPs with oxygen self-generating capacity simultaneously displayed PTT and PDT effects upon NIR irradiation, resulting in a remarkable enhancement of the phototherapeutic efficacy. Furthermore, the combined application of triple imaging (FLI, PTI, and PAI)-guided strategies achieved the synergistic treatment effects of phototherapy (PTT and PDT) and chemotherapy, resulting in improved antitumor activity and no detectable side effects. Therefore, this study may set a precedent in the development of an easy-to-use and versatile nanoplatform for synergistic phototheranostics against cancer, and build a steady foundation for the medical implementation of nanotheranostics.

Acknowledgments

This work was supported by the National Natural Science Foundation of China (82072060, 81773685, and 81571807), the Fundamental Research Funds for the Central Universities (XDJK2019TY002, China), the Chengdu Science and Technology Program (2018-CY02-00042-GX, China), the 1.3.5 Project for Disciplines of Excellence, West China Hospital, Sichuan University (ZYYC21002, ZYJC18032and ZY2016101, China), the Natural Science Foundation Project of Chongqing (cstc2020jcyj-msxmX0292, China), and the Venture & Innovation Support Program for Chongqing Overseas Returnees (cx2018029, China).

Author contributions

Shuangquan Gou, Nanxi Chen, and Xiaoai Wu contributed equally as joint first author. Bowen Ke and Bo Xiao designed experiments, supervised studies, and wrote the manuscript. Shuangquan Gou, Nanxi Chen, Xiaoai Wu, Menghang Zu, and Shixiong Yi performed the experiments. Binwu Ying, Fangyin Dai, Bowen Ke, and Bo Xiao edited and revised the manuscript. All authors have given approval to the final version of the manuscript.

Conflicts of interest

The authors have no conflicts of interest to declare.

Appendix A. Supporting information

Supporting data to this article can be found online at https://doi.org/10.1016/j.apsb.2021.07.001.

References

1. Mura S, Nicolas J, Couvreur P. Stimuli-responsive nanocarriers for drug delivery. *Nat Mater* 2013;**12**:991−1003.
2. Choi KY, Han HS, Lee ES, Shin JM, Almquist BD, Lee DS, et al. Hyaluronic acid-based activatable nanomaterials for stimuli-responsive imaging and therapeutics: beyond CD44-mediated drug delivery. *Adv Mater* 2019;**31**:e1803549.
3. Li Z, Song N, Yang YW. Stimuli-responsive drug-delivery systems based on supramolecular nanovalves. *Matter* 2019;**1**:345−68.
4. Yin W, Ke W, Chen W, Xi L, Zhou Q, Mukerabigwi JF, et al. Integrated block copolymer prodrug nanoparticles for combination of tumor oxidative stress amplification and ROS-responsive drug release. *Biomaterials* 2019;**195**:63−74.
5. Yin W, Ke W, Lu N, Wang Y, Japir AMM, Mohammed F, et al. Glutathione and reactive oxygen species dual-responsive block copolymer prodrugs for boosting tumor site-specific drug release and enhanced antitumor efficacy. *Biomacromolecules* 2020;**21**:921−9.
6. Kelley EG, Albert JNL, Sullivan JNL, Epps TH. Stimuli-responsive copolymer solution and surface assemblies for biomedical applications. *Chem Soc Rev* 2013;**42**:7057−71.

7. Li LL, Xing H, Zhang JJ, Lu Y. Functional DNA molecules enable selective and stimuli-responsive nanoparticles for biomedical applications. *Accounts Chem Res* 2019;**52**:2415−26.
8. Altman GH, Diaz F, Jakuba C, Calabro T, Horan RL, Chen J, et al. Silk-based biomaterials. *Biomaterials* 2003;**24**:401−16.
9. Lammel AS, Hu X, Park SH, Kaplan DL, Scheibel TR. Controlling silk fibroin particle features for drug delivery. *Biomaterials* 2010;**31**:4583−91.
10. Seib FP, Jones TG, Rnjak-Kovacina J, Lin Y, Kaplan DL. pH-Dependent anticancer drug release from silk nanoparticles. *Adv Healthc Mater* 2013;**2**:1606−11.
11. Gou S, Huang Y, Wan Y, Ma Y, Zhou X, Tong X, et al. Multi-bioresponsive silk fibroin-based nanoparticles with on-demand cytoplasmic drug release capacity for CD44-targeted alleviation of ulcerative colitis. *Biomaterials* 2019;**212**:39−54.
12. Gou S, Huang Y, Sung J, Xiao B, Merlin D. Silk fibroin-based nanotherapeutics: application in the treatment of colonic diseases. *Nanomedicine* 2019;**14**:2373−8.
13. De Palma M, Hanahan D. The biology of personalized cancer medicine: facing individual complexities underlying hallmark capabilities. *Mol Oncol* 2012;**6**:111−27.
14. Xiao B, Viennois E, Chen Q, Wang L, Han MK, Zhang Y, et al. Silencing of intestinal glycoprotein CD98 by orally targeted nanoparticles enhances chemosensitization of colon cancer. *ACS Nano* 2018;**12**:5253−65.
15. Chen Q, Wen J, Li H, Xu Y, Liu F, Sun S. Recent advances in different modal imaging-guided photothermal therapy. *Biomaterials* 2016;**106**:144−66.
16. Li J, Cui D, Jiang Y, Huang J, Cheng P, Pu K. Near-infrared photoactivatable semiconducting polymer nanoblockaders for metastasis-inhibited combination cancer therapy. *Adv Mater* 2019;**31**:e1905091.
17. Luo D, Carter KA, Miranda D, Lovell JF. Chemophototherapy: an emerging treatment option for solid tumor. *Adv Sci* 2017;**4**:1600106.
18. Wan G, Chen B, Li L, Wang D, Shi S, Zhang T, et al. Nanoscaled red blood cells facilitate breast cancer treatment by combining photothermal/photodynamic therapy and chemotherapy. *Biomaterials* 2018;**155**:25−40.
19. Chen S, Lei Q, Qiu W, Liu L, Zheng D, Fan J, et al. Mitochondria-targeting "nanoheater" for enhanced photothermal/chemo-therapy. *Biomaterials* 2017;**117**:92−104.
20. Kasahara A, Scorrano L. Mitochondria: from cell death executioners to regulators of cell differentiation. *Trends Cell Biol* 2014;**24**:761−70.
21. Xu L, Tong G, Song Q, Zhu C, Zhang H, Shi J, et al. Enhanced intracellular Ca^{2+} nanogenerator for tumor-specific synergistic therapy *via* disruption of mitochondrial Ca^{2+} homeostasis and photothermal therapy. *ACS Nano* 2018;**12**:6806−16.
22. Pan LM, Liu JA, Shi JL. Intranuclear photosensitizer delivery and photosensitization for enhanced photodynamic therapy with ultralow irradiance. *Adv Funct Mater* 2014;**24**:7318−27.
23. Yu ZZ, Sun QQ, Pan W, Li N, Tang B. An near-infrared triggered nanophotosensitizer inducing domino effect on mitochondrial reactive oxygen Species burst for cancer therapy. *ACS Nano* 2015;**9**:11064−74.
24. Jung HS, Han J, Lee J, Choi J, Kweon HS, Kim J, et al. Enhanced NIR radiation-triggered hyperthermia by mitochondrial targeting. *J Am Chem Soc* 2015;**137**:3017−23.
25. Zhang DD, Wen L, Huang R, Wang H, Hu X, Xing D. Mitochondrial specific photodynamic therapy by rare-earth nanoparticles mediated near-infrared graphene quantum dots. *Biomaterials* 2018;**153**:14−26.
26. Wang H, Gao Z, Liu X, Agarwal P, Zhao S, Conroy DW, et al. Targeted production of reactive oxygen species in mitochondria to overcome cancer drug resistance. *Nat Commun* 2018;**9**:562.
27. Wang Y, Luo S, Zhang C, Liao X, Lui T, Jiang Z, et al. An NIR-fluorophore-based therapeutic endoplasmic reticulum stress inducer. *Adv Mater* 2018;**30**:1800475.
28. Zhang X, Huang Y, Song H, Canup BSB, Gou S, She Z, et al. Inhibition of growth and lung metastasis of breast cancer by tumor-homing triple-bioresponsive nanotherapeutics. *J Control Release* 2020;**328**:454−69.
29. Wang S, Yu GC, Wang ZT, Jacobson O, Tian R, Lin LS, et al. Hierarchical tumor microenvironment-responsive nanomedicine for programmed delivery of chemotherapeutics. *Adv Mater* 2018;**30**:1803926.
30. Tao H, Hwang B, Marelli B, Yang M, Brenckle MA, Kim S, et al. Silk-based resorbable electronic devices for remotely controlled therapy and *in vivo* infection abatement. *Proc Natl Acad Sci U S A* 2014;**111**:17385−9.
31. Wenk E, Merkle HP, Meinel L. Silk fibroin as a vehicle for drug delivery applications. *J Control Release* 2011;**150**:128−41.
32. Wang D, Xue B, Ohulchanskyy TY, Liu Y, Yakovliev A, Ziniuk R, et al. Inhibiting tumor oxygen metabolism and simultaneously generating oxygen by intelligent upconversion nanotherapeutics for enhanced photodynamic therapy. *Biomaterials* 2020;**251**:120088.
33. Wu CA, Chao Y, Shiah SG, Lin WW. Nutrient deprivation induces the Warburg effect through ROS/AMPK-dependent activation of pyruvate dehydrogenase kinase. *BBA-Mol Cell Res* 2013;**1833**:1147−56.
34. Xiao WY, Wang P, Ou C, Huang X, Tang Y, Wu M, et al. 2-Pyridone-functionalized Aza-BODIPY photosensitizer for imaging-guided sustainable phototherapy. *Biomaterials* 2018;**183**:1−9.
35. Zhu S, Gu Y, Zhao L. Harnessing tumor microenvironment for nanoparticle-mediated radiotherapy. *Adv Ther* 2018;**1**:1800050.
36. Chen XH, Li Y, Gao M, Ren L, Tang BZ. Mitochondria and lysosomes-targeted synergistic chemo-photodynamic therapy associated with self-monitoring by dual light-up fluorescence. *Adv Funct Mater* 2018;**28**:1804362.
37. Gao P, Pan W, Li N, Tang B. Boosting cancer therapy with organelle-targeted nanomaterials. *ACS Appl Mater Interfaces* 2019;**11**:26529−58.
38. Xu T, Ma Y, Yuan Q, Hu H, Hu X, Qian Z, et al. Enhanced ferroptosis by oxygen-boosted phototherapy based on a 2-in-1 nanoplatform of ferrous hemoglobin for tumor synergistic therapy. *ACS Nano* 2020;**14**:3414−25.